Exact exchange plane-wave-pseudopotential calculations for slabs: Extending the width of the vacuum

Eberhard Engel

Center for Scientific Computing, J.W.Goethe-Universität Frankfurt, Max-von-Laue-Str. 1 D-60438 Frankfurt/Main, Germany

Standard plane-wave pseudopotential (PWPP) calculations for slabs such as graphene become extremely demanding, as soon as the exact exchange (EXX) of density functional theory is applied. Even if the Krieger-Li-Iafrate (KLI) approximation for the EXX potential is utilized, such EXX-PWPP calculations suffer from the fact that an accurate representation of the occupied states throughout the complete vacuum between the replicas of the slab is required. In this contribution, a robust and efficient extension scheme for the PWPP states is introduced, which ensures the correct exponential decay of the slab states in the vacuum for standard cutoff energies and therefore facilitates EXX-PWPP calculations for very wide vacua and rather thick slabs. Using this scheme, it is explicitly verified that the Slater component of the EXX/KLI potential decays as $-1/z$ over an extended region sufficiently far from the surface (assumed to be perpendicular to the z direction) and from the middle of the vacuum, thus reproducing the asymptotic behavior of the exact EXX potential of a single slab. The calculations also reveal that the orbital-shift component of the EXX/KLI potential is quite sizable in the asymptotic region. In spite of the long-range exchange potential, the replicas of the slab decouple rather quickly with increasing width of the vacuum. Relying on the identity of the work function with the Fermi energy obtained with a suitably normalized total potential, the present EXX/KLI calculations predict work functions for both graphene and the Si(111) surface which are substantially larger than the corresponding experimental data. Together with the size of the orbital-shift potential in the asymptotic region, the very large EXX/KLI work functions indicate a failure of the KLI approximation for nonmetallic slabs.

I. INTRODUCTION

The exchange-correlation (xc) potential v_{xc} at the surface of a solid is the most important quantity when calculating its work function or ionization potential using density functional theory (DFT). Renewed interest in the xc potential at surfaces [1–20] has been triggered by the observation that the exact exchange (EXX) potential v_x of DFT often differs qualitatively from the potentials produced by conventional density functionals, such as the local density approximation (LDA) or the generalized gradient approximation (GGA). Most importantly, the exact v_x of finite systems falls off as $-e^2/r$ for large distance r from the system [21], in contrast to the exponential decay of the corresponding LDA/GGA potentials. In addition, EXX-based approaches often yield clear improvements over LDA/GGA functionals [22–45].

In DFT calculations, surfaces are often modeled in terms of slabs. If sufficiently many atomic layers are included in the slab, its surface provides a rather realistic account of the surface of the corresponding bulk material. If necessary, quantities like the work function can be extrapolated to infinite thickness on the basis of several slab calculations for different slab thicknesses. However, slabs are also of interest in themselves, the most prominent example being single-layer graphene.

The exact v_x and the corresponding EXX energy density e_x have been studied for both jellium slabs and semi-infinite jellium by Sahni and collaborators [1–5] as well as Horowitz and collaborators [6–9,11]. They showed [5,6] that the exact v_x of jellium slabs behaves as $-e^2/z$ far outside the surface, if the

electrons are confined to the region $-L < z < L$. Consistent with the physical origin of this result, the self-interaction correction terms in the EXX functional, the exact e_x falls off as $-e^2n/(2z)$, where n denotes the electron density [7]. As demonstrated later [12,13], both results also apply to nonjellium slabs, for which one has a Bravais lattice in the xy directions, rather than full translational symmetry,

$$e_x(\boldsymbol{r}) \xrightarrow{z\gg L} -\frac{e^2 n(\boldsymbol{r})}{2z}, \tag{1}$$

$$v_x(\boldsymbol{r}) \xrightarrow{z\gg L} -\frac{e^2}{z} \tag{2}$$

(irrespective of the band structure of the slabs).

DFT calculations for slabs are often performed with the plane-wave pseudopotential (PWPP) approach (see, e.g., Ref. [46]), which implies that the slab under consideration is periodically repeated along the z direction [47]. The width $\bar{d}$ of the vacuum between the replicas of the slab and thus the width d of the 3D unit cell (referred to as supercell) has to be chosen sufficiently large, so that the replicas do not interact with each other. The width required for a decoupling depends on the range of the states and the Kohn-Sham (KS) potential outside the surface of the slab. Since in this region the states decay exponentially into the vacuum, local and semilocal xc functionals, such as the LDA or GGA, lead to an exponential decay of the xc potential. At the same time, the ionic potential and the Hartree potential of the electrons

cancel each other outside the surface region, as long as there is no net macroscopic surface charge. For this reason often quite moderate $\bar{d}$ are sufficient for LDA/GGA calculations.

In practice, the plane-wave representation reproduces the exponential decay of the KS states into the vacuum only over a limited range. In the rest of the vacuum the PWPP states oscillate around zero, with amplitudes whose size depends on how far out the plane-wave expansion can follow the exponential decay for given cutoff energy. While this numerical noise is irrelevant for LDA/GGA calculations, the same is not true for the EXX approach. This is most obvious if the Krieger-Li-Iafrate (KLI) approximation [48] is employed for determining the EXX potential [21,49–52]. Its main component, the Slater potential, is the ratio of the local exchange energy density and the density, $v_{\text{Slater}}(\boldsymbol{r}) = 2e_{\text{x}}(\boldsymbol{r})/n(\boldsymbol{r})$, which is extremely sensitive to numerical noise in the states. For this reason only quite limited $\bar{d}$ could be realized in the first EXX-PWPP calculations for slabs in Ref. [12], in spite of the excessive cutoff energies utilized in this work.

Due to the limited $\bar{d}$, the EXX-PWPP results of Ref. [12] did not allow to draw definitive conclusions on the properties of the EXX approach. Even for the simplest slab, graphene, only the onset of the $-1/z$ behavior of v_{Slater} far outside the slab, predicted by (1), could be observed. Moreover, while the results for graphene indicated that a decoupling of the replicas might be reached for values of $\bar{d}$ not much larger than those used for LDA/GGA calculations, this early decoupling needs to be substantiated by calculations for larger $\bar{d}$ and slabs of nonzero thickness.

In this contribution, an extension scheme for the KS states in the vacuum is introduced which allows EXX-PWPP calculations for very large $\bar{d}$ and standard cutoff energies, thereby resolving the limitations of Ref. [12]. The extension scheme is based on the analytical form of the states of a single slab in the vacuum. These states are matched to the numerical PWPP states at a suitable matching point sufficiently far outside the surface. The resulting real-space states are then used to calculate $e_{\text{x}}(\boldsymbol{r})$, $n(\boldsymbol{r})$, and all other components of the EXX potential in the KLI approximation. Due to the clean asymptotic behavior of all components, the KLI potential can be reliably calculated for $\bar{d}$ as large as 500 Bohr. The computational efficiency of the approach is demonstrated by EXX/KLI calculations for graphene and several Si(111) slabs, including an 18-layer Si(111) slab.

The paper is organized as follows. In Sec. II, the behavior of the states of an isolated slab far outside the surface is analyzed in detail, extending the discussion of Refs. [12,13] to the next-to-leading order. The asymptotic behavior of the states of an isolated slab is then used to correct the numerical PWPP states for repeated slabs in the vacuum region (Sec. III). Section IV summarizes the KLI approximation for an isolated slab. Section V addresses the numerical implementation of the extension scheme, introducing several variants, which differ in accuracy and computational efficiency. All numerical results are provided in Sec. VI. In Secs. VI A and VI B, the quality of the extension scheme is investigated, comparing the different variants. On this basis, Secs. VI C–VI E then deal with the properties of the EXX/KLI potential. Finally, Sec. VII summarizes the results and offers some conclusions.

Since $\bar{d}$ and d only differ by the fixed thickness of the slab, the width of the vacuum will often be addressed in terms of d in the following. Atomic units are used throughout this work, unless explicitly stated otherwise.

II. ASYMPTOTIC BEHAVIOR OF STATES OF SINGLE SLAB

Consider a total KS potential v_{s}, which is periodic in the xy directions, while it confines the electrons to the finite range $-L < z < L$ in z direction,

$$v_{\text{s}}(\boldsymbol{r}) = \sum_{\boldsymbol{G}} e^{i\boldsymbol{G}\cdot\boldsymbol{r}_{\parallel}} v(\boldsymbol{G},z). \tag{3}$$

Here, $\boldsymbol{r}_{\parallel} = (x,y)$ and $\boldsymbol{G}$ is a vector of the 2D reciprocal lattice in the xy directions. The corresponding KS states have the form

$$\phi_{\boldsymbol{k}\alpha}(\boldsymbol{r}) = \frac{e^{i\boldsymbol{k}\cdot\boldsymbol{r}_{\parallel}}}{\sqrt{A}} \sum_{\boldsymbol{G}} e^{i\boldsymbol{G}\cdot\boldsymbol{r}_{\parallel}} c_{\boldsymbol{k}\alpha}(\boldsymbol{G},z), \tag{4}$$

where $\boldsymbol{k}$ is the 2D crystal momentum. The normalization is chosen so that $c_{\boldsymbol{k}\alpha}$ integrates up to 1 for a single 2D unit cell of area A,

$$\delta_{\alpha,\alpha'} = \int_{-\infty}^{\infty} dz \sum_{\boldsymbol{G}} c_{\boldsymbol{k}\alpha}^{*}(\boldsymbol{G},z) c_{\boldsymbol{k}\alpha'}(\boldsymbol{G},z). \tag{5}$$

The coefficients $c_{\boldsymbol{k}\alpha}$ satisfy the KS equations on the reciprocal lattice,

$$\frac{(\boldsymbol{G}+\boldsymbol{k})^2 - \partial_z^2}{2} c_{\boldsymbol{k}\alpha}(\boldsymbol{G},z) + \sum_{\boldsymbol{G}'} v(\boldsymbol{G}-\boldsymbol{G}',z) c_{\boldsymbol{k}\alpha}(\boldsymbol{G}',z)$$

$$= \epsilon_{\boldsymbol{k}\alpha} c_{\boldsymbol{k}\alpha}(\boldsymbol{G},z). \tag{6}$$

In Ref. [13], it has been shown that for the slab geometry under consideration the exact exchange potential v_{x} behaves as $-1/z$ for $z \to \infty$. The same applies to the Slater component of the KLI approximation for the EXX potential [12]. In addition, one finds [53] that, in general, the next-to-leading order in the Slater potential has the form $-w/z^2$. In the following, $v_{\text{s}}(\boldsymbol{r})$ is therefore assumed to have the asymptotic form

$$v_{\text{s}}(\boldsymbol{r}) \xrightarrow{z \to \infty} -\frac{u}{z} + \delta v(z) + \dots. \tag{7}$$

$\delta v(z)$ could represent the potential $-w/z^2$, but also other correction terms to $-u/z$. On the reciprocal lattice, one then has

$$v(\boldsymbol{G},z) \xrightarrow{z \to \infty} \delta_{\boldsymbol{G},0}\left[-\frac{u}{z} + \delta v(z)\right]. \tag{8}$$

All components of $v(\boldsymbol{G},z)$ with nonvanishing $\boldsymbol{G}$ decay faster than $1/z$.

In the following, the differential equation (6) is analyzed for large z. The solution of this equation is complicated by the fact that the amplitudes for different $\boldsymbol{G}$ are coupled by the potential. In order to clarify their asymptotic behavior, we first assume that for large z all amplitudes have exactly the same z dependence,

$$c(\boldsymbol{G},z) \xrightarrow{z \to \infty} a(\boldsymbol{G})\,b(z)$$

(in the rest of this section the dependence of all quantities on $\boldsymbol{k}\alpha$ is omitted for brevity—only a single state is considered). Under this assumption, all terms in the sum over $\boldsymbol{G}'$ on the right-hand side of (6) with $\boldsymbol{G}' \neq \boldsymbol{G}$ are suppressed by the factor $v(\boldsymbol{G} - \boldsymbol{G}',z)/v(\boldsymbol{0},z)$, so that (6) reduces to the homogeneous differential equation

$$\partial_z^2 c_{\mathrm{h}}(\boldsymbol{G},z) = [(\boldsymbol{G} + \boldsymbol{k})^2 - 2\epsilon + 2v(\boldsymbol{0},z)]c_{\mathrm{h}}(\boldsymbol{G},z). \quad (9)$$

To leading order, the solutions of this equation with the asymptotic potential (8) have the form

$$c_{\mathrm{h}}(\boldsymbol{G},z) = f_0(\boldsymbol{G})\,\bar{c}_{\mathrm{h}}(\boldsymbol{G},z), \quad (10)$$

$$\bar{c}_{\mathrm{h}}(\boldsymbol{G},z) \xrightarrow{z \to \infty} z^{u/\gamma(\boldsymbol{G})}\,e^{-\gamma(\boldsymbol{G})z}, \quad (11)$$

with

$$\gamma(\boldsymbol{G}) = [(\boldsymbol{G} + \boldsymbol{k})^2 - 2\epsilon]^{1/2}. \quad (12)$$

One thus ends up with a contradiction, since the z dependence of the solutions (10) obviously varies with $\boldsymbol{G}$.

In the second step, we analyze whether one can have a finite number of $c(\boldsymbol{G},z)$ which decay in exactly the same way, while all other amplitudes fall off faster. The differential equation for the set of asymptotically dominant amplitudes is identical with (9), since the terms in (6) with $\boldsymbol{G}' \neq \boldsymbol{G}$ are again at least suppressed by the factor $v(\boldsymbol{G} - \boldsymbol{G}',z)/v(\boldsymbol{0},z)$. The asymptotically dominant amplitudes therefore have the form (10). In order for them to show the same z dependence, all $\gamma(\boldsymbol{G})$ of this set have to be identical. This is obviously only possible for $\boldsymbol{k}$-points on the boundary of the first Brillouin zone (BZ): for these $\boldsymbol{k}$, one finds one $\boldsymbol{G}$-vector with $(\boldsymbol{G} + \boldsymbol{k})^2 = \boldsymbol{k}^2$. As soon as $\boldsymbol{k}$ belongs to the interior of the first BZ, the condition $(\boldsymbol{G} + \boldsymbol{k})^2 = \boldsymbol{k}^2$ can no longer be satisfied. Consequently, there is one amplitude that decays more slowly than all others. From Eqs. (10)–(12), this asymptotically leading amplitude is easily identified as $c(\boldsymbol{0},z)$.

As soon as one wants to determine the z dependence of $c(\boldsymbol{G},z)$ beyond the asymptotically leading term, the coupling of different $\boldsymbol{G}$ can no longer be neglected. Quite generally, the solution of (6) can be expressed as [54]

$$c(\boldsymbol{G},z) = c_{\mathrm{h}}(\boldsymbol{G},z) + 2\sum_{\boldsymbol{G}' \neq \boldsymbol{G}} \int_{z_1}^{z_2} dz'\,\mathcal{G}(\boldsymbol{G},z,z')$$
$$\times\, v(\boldsymbol{G} - \boldsymbol{G}',z')\,c(\boldsymbol{G}',z'), \quad (13)$$

where $\mathcal{G}(\boldsymbol{G},z,z')$ is the Green's function corresponding to (9). Equation (13) is valid in the range $z_1 < z < z_2$. However, the boundaries can be chosen freely, as long as the z' integral in (13) exists and $c(\boldsymbol{G},z)$ remains normalizable. If $q_{\mathrm{h}}(\boldsymbol{G},z)$ denotes the second, non-normalizable solution of (9), $\mathcal{G}$ can be written as

$$\mathcal{G}(\boldsymbol{G},z,z') = \Theta(z - z')\,\bar{c}_{\mathrm{h}}(\boldsymbol{G},z)\,q_{\mathrm{h}}(\boldsymbol{G},z')$$
$$+ \Theta(z' - z)\,q_{\mathrm{h}}(\boldsymbol{G},z)\,\bar{c}_{\mathrm{h}}(\boldsymbol{G},z'), \quad (14)$$

with the normalization of $q_{\mathrm{h}}(\boldsymbol{G},z)$ determined by

$$q_{\mathrm{h}}(\boldsymbol{G},z)\,\partial_z\bar{c}_{\mathrm{h}}(\boldsymbol{G},z) - \bar{c}_{\mathrm{h}}(\boldsymbol{G},z)\,\partial_z q_{\mathrm{h}}(\boldsymbol{G},z) = 1. \quad (15)$$

For large z, the leading contribution to $q_{\mathrm{h}}(\boldsymbol{G},z)$ is easily specified,

$$q_{\mathrm{h}}(\boldsymbol{G},z) \xrightarrow{z \to \infty} \frac{-1}{2\gamma(\boldsymbol{G})}\,z^{-u/\gamma(\boldsymbol{G})}\,e^{\gamma(\boldsymbol{G})z}, \quad (16)$$

so that $\mathcal{G}$ is known in the asymptotic region.

Now consider the solution (13) for the most weakly decaying amplitude(s), so that $\gamma(\boldsymbol{G}) \leqslant \gamma(\boldsymbol{G}')$. If both z and z_1 are sufficiently large, all contributions to the second term on the right-hand side of (13) can be rewritten as

$$2\int_{z_1}^{\infty} dz'\,\mathcal{G}(\boldsymbol{G},z,z')\,v(\boldsymbol{G} - \boldsymbol{G}',z')\,c(\boldsymbol{G}',z')$$

$$\xrightarrow{z \to \infty} -\frac{1}{\gamma(\boldsymbol{G})}\int_{z_1}^{z} dz'\,\bar{c}_{\mathrm{h}}(\boldsymbol{G},z)\,\frac{c(\boldsymbol{G}',z')}{\bar{c}_{\mathrm{h}}(\boldsymbol{G},z')}\,v(\boldsymbol{G} - \boldsymbol{G}',z')$$
$$-\frac{1}{\gamma(\boldsymbol{G})}\int_{z}^{\infty} dz'\,\frac{\bar{c}_{\mathrm{h}}(\boldsymbol{G},z')}{\bar{c}_{\mathrm{h}}(\boldsymbol{G},z)}c(\boldsymbol{G}',z')\,v(\boldsymbol{G} - \boldsymbol{G}',z')$$

$$= -\frac{1}{\gamma(\boldsymbol{G})}\,\bar{c}_{\mathrm{h}}(\boldsymbol{G},z)\int_{z_1}^{\infty} dz'\,\frac{c(\boldsymbol{G}',z')}{\bar{c}_{\mathrm{h}}(\boldsymbol{G},z')}\,v(\boldsymbol{G} - \boldsymbol{G}',z')$$
$$+\frac{1}{\gamma(\boldsymbol{G})}\,\bar{c}_{\mathrm{h}}(\boldsymbol{G},z)\int_{z}^{\infty} dz'\,\frac{c(\boldsymbol{G}',z')}{\bar{c}_{\mathrm{h}}(\boldsymbol{G},z')}\,v(\boldsymbol{G} - \boldsymbol{G}',z')$$
$$-\frac{1}{\gamma(\boldsymbol{G})}\int_{z}^{\infty} dz'\,\frac{\bar{c}_{\mathrm{h}}(\boldsymbol{G},z')}{\bar{c}_{\mathrm{h}}(\boldsymbol{G},z)}c(\boldsymbol{G}',z')\,v(\boldsymbol{G} - \boldsymbol{G}',z'),$$

since (i) all $c(\boldsymbol{G}',z')$ decay at least as fast as $\bar{c}_{\mathrm{h}}(\boldsymbol{G},z')$ and (ii) $v(\boldsymbol{G} - \boldsymbol{G}',z')$ falls off faster than $1/z$. The first term on the right-hand side of this equation, however, is simply a constant times the solution of the homogeneous equation and can be absorbed into the first term on the right-hand side of Eq. (13). The remaining terms fall off as

$$\bar{c}_{\mathrm{h}}(\boldsymbol{G},z)\int_{z}^{\infty} dz'\,v(\boldsymbol{G} - \boldsymbol{G}',z'),$$

if $c(\boldsymbol{G}',z')$ decays as fast as $\bar{c}_{\mathrm{h}}(\boldsymbol{G},z')$ (which is only possible for $\boldsymbol{k}$ on the boundary of the first BZ), or even faster for all other $\boldsymbol{G}'$. Consequently, Eq. (13) allows for iteration in the case of the most weakly decaying amplitudes. In practice, only the first-order corrections to $c_{\mathrm{h}}(\boldsymbol{G},z)$ are relevant, so that one can replace $c(\boldsymbol{G},z)$ on the right-hand side of (13) by $f_0(\boldsymbol{G})\bar{c}_{\mathrm{h}}(\boldsymbol{G},z)$.

In the case of all other amplitudes, there exist $c(\boldsymbol{G}',z')$, which decay more slowly than $\bar{c}_{\mathrm{h}}(\boldsymbol{G},z')$. For large z, the right-hand side of (13) is dominated by the contribution(s) of the most weakly decaying amplitude(s) to the sum over $\boldsymbol{G}'$. If $\boldsymbol{G}'$ corresponds to the most weakly decaying amplitude(s), one finds to leading order

$$\int_{z_1}^{z} dz'\,\bar{c}_{\mathrm{h}}(\boldsymbol{G},z)\,\frac{c(\boldsymbol{G}',z')}{\bar{c}_{\mathrm{h}}(\boldsymbol{G},z')}\,v(\boldsymbol{G} - \boldsymbol{G}',z')$$

$$\xrightarrow{z \to \infty} f_0(\boldsymbol{G}')\,\bar{c}_{\mathrm{h}}(\boldsymbol{G},z)\int_{z_1}^{z} dz'\,\frac{\bar{c}_{\mathrm{h}}(\boldsymbol{G}',z')}{\bar{c}_{\mathrm{h}}(\boldsymbol{G},z')}\,v(\boldsymbol{G} - \boldsymbol{G}',z')$$

$$\xrightarrow{z \to \infty} \frac{c_{\mathrm{h}}(\boldsymbol{G}',z)\,v(\boldsymbol{G} - \boldsymbol{G}',z)}{\gamma(\boldsymbol{G}) - \gamma(\boldsymbol{G}')} + \mathrm{const} \times \bar{c}_{\mathrm{h}}(\boldsymbol{G},z)$$

and

$$\int_z^\infty dz' \, \frac{\bar{c}_{\rm h}(\boldsymbol{G},z')}{\bar{c}_{\rm h}(\boldsymbol{G},z)} c(\boldsymbol{G}',z') \, v(\boldsymbol{G} - \boldsymbol{G}',z')$$

$$\xrightarrow{z\to\infty} f_0(\boldsymbol{G}') \int_z^\infty dz' \, \frac{\bar{c}_{\rm h}(\boldsymbol{G},z')}{\bar{c}_{\rm h}(\boldsymbol{G},z)} \bar{c}_{\rm h}(\boldsymbol{G}',z') \, v(\boldsymbol{G} - \boldsymbol{G}',z')$$

$$\xrightarrow{z\to\infty} \frac{c_{\rm h}(\boldsymbol{G}',z) \, v(\boldsymbol{G} - \boldsymbol{G}',z)}{\gamma(\boldsymbol{G}) + \gamma(\boldsymbol{G}')}.$$

Consequently, the leading contribution to $c(\boldsymbol{G},z)$ is suppressed by the factor $v(\boldsymbol{G} - \boldsymbol{G}',z)$ compared to $c(\boldsymbol{G}',z)$. As a result, iteration of (13) is again legitimate and can be restricted to first order (see Supplemental Material [55]).

The asymptotically dominant contributions to all $c(\boldsymbol{G},z)$ are thus obtained from

$$c(\boldsymbol{G},z) = f_0(\boldsymbol{G})\bar{c}_{\rm h}(\boldsymbol{G},z) + \sum_{\boldsymbol{G}'\neq\boldsymbol{G}} f_0(\boldsymbol{G}')\bar{c}_{\rm i}(\boldsymbol{G},\boldsymbol{G}',z), \quad (17)$$

with

$$\bar{c}_{\rm i}(\boldsymbol{G},\boldsymbol{G}',z) = -\frac{1}{\gamma(\boldsymbol{G})} \int_{z_1}^z dz' \, \frac{\bar{c}_{\rm h}(\boldsymbol{G},z)}{\bar{c}_{\rm h}(\boldsymbol{G},z')} \, \bar{c}_{\rm h}(\boldsymbol{G}',z')$$

$$\times \, v(\boldsymbol{G} - \boldsymbol{G}',z')$$

$$- \frac{1}{\gamma(\boldsymbol{G})} \int_z^\infty dz' \, \frac{\bar{c}_{\rm h}(\boldsymbol{G},z')}{\bar{c}_{\rm h}(\boldsymbol{G},z)} \, \bar{c}_{\rm h}(\boldsymbol{G}',z')$$

$$\times \, v(\boldsymbol{G} - \boldsymbol{G}',z). \quad (18)$$

If the amplitudes $c(\boldsymbol{G},z)$ are known at some point z_0, Eq. (17) represents a set of linear equations for the coefficients $f_0(\boldsymbol{G})$.

In the case of the asymptotically leading amplitude(s), the corrections $\bar{c}_{\rm i}(\boldsymbol{G},\boldsymbol{G}',z)$ decay faster than the dominant term $\bar{c}_{\rm h}(\boldsymbol{G},z)$ by at least a factor of $1/z$, resulting from $\int_z^\infty dz' v(\boldsymbol{G} - \boldsymbol{G}',z')$. Inclusion of the corrections in the asymptotic state is only meaningful if also $c_{\rm h}(\boldsymbol{G},z)$ is handled correctly to this order. In order to determine $c_{\rm h}(\boldsymbol{G},z)$ more completely, one has to consider the homogeneous asymptotic differential equation with δv taken into account,

$$\partial_z^2 c_{\rm h}(\boldsymbol{G},z) = \left[\gamma^2(\boldsymbol{G}) - \frac{2u}{z} + 2\delta v(z)\right] c_{\rm h}(\boldsymbol{G},z). \quad (19)$$

If the ultimately dominant behavior (11) is factorized out of the solutions of (19),

$$c_{\rm h}(\boldsymbol{G},z) = f(\boldsymbol{G},z) \, z^{u/\gamma(\boldsymbol{G})} \, e^{-\gamma(\boldsymbol{G})z}, \quad (20)$$

one arrives at the differential equation

$$0 = \partial_z^2 f(\boldsymbol{G},z) + 2\left[\frac{u}{\gamma(\boldsymbol{G})z} - \gamma(\boldsymbol{G})\right]\partial_z f(\boldsymbol{G},z)$$

$$+ \left[\frac{u}{\gamma(\boldsymbol{G})}\left(\frac{u}{\gamma(\boldsymbol{G})} - 1\right)\frac{1}{z^2} - 2\delta v(z)\right] f(\boldsymbol{G},z). \quad (21)$$

A rigorous solution of (21) requires a numerical inward integration of $f(\boldsymbol{G},z)$, starting with $f(\boldsymbol{G},z_\infty) = 1$ at some suitable (large) point z_∞ and fixing the normalization by solution of (17) at the end point z_0 of the inward integration.

This procedure is, however, not really necessary to obtain accurate wave functions. As long as $|\delta v| \ll \gamma^2$ and $|\partial_z \delta v| \ll \gamma|\delta v|$, the solution of (21) is, to leading order in the correction,

given by

$$f(\boldsymbol{G},z) = f_0(\boldsymbol{G})\left(1 + \frac{u[\gamma(\boldsymbol{G}) - u]}{2\gamma^3(\boldsymbol{G})z}\right)$$

$$\times \exp\left[\frac{1}{\gamma(\boldsymbol{G})} \int_z^{z_\infty} dz' \, \delta v(z')\right]. \quad (22)$$

One finds that the condition $|\partial_z \delta v| \ll \gamma|\delta v|$ is well satisfied for the slabs considered in this contribution.

To summarize, the asymptotic solutions of the coupled KS equations (6) are given by Eqs. (17) and (18). Equation (17) accounts in particular for (i) the coupling of all amplitudes with $\boldsymbol{G} \neq \boldsymbol{0}$ to the asymptotically dominant amplitude with $\boldsymbol{G} = \boldsymbol{0}$ in the case of all states well inside the first BZ, and (ii) the coupling of the two asymptotically dominant amplitudes in the case of states on the boundary of the first BZ (or very close to it). If the core element of these equations, the non-normalized solution $\bar{c}_{\rm h}$ of the homogeneous differential equation (9) is calculated from Eqs. (20) and (22), the result of (17) also includes the leading corrections to the ultimate asymptotic form (11) of the amplitudes.

III. EXTENSION OF 3D BLOCH STATES INTO VACUUM

In supercell calculations with repeated slabs, the Bloch states are represented as

$$\phi_{\boldsymbol{k}k_z\alpha}(\boldsymbol{r}) = \frac{e^{i\boldsymbol{k}\cdot\boldsymbol{r}_\parallel + ik_z z}}{\sqrt{\Omega}} \sum_{\boldsymbol{G},G_z} e^{i\boldsymbol{G}\cdot\boldsymbol{r}_\parallel + iG_z z} c_{\boldsymbol{k}k_z\alpha}(\boldsymbol{G},G_z), \quad (23)$$

where Ω denotes the volume of the supercell. In the following, the supercell is assumed to have the extension d in z direction ($\Omega = Ad$) and to have its center at the center of the slab. If d and therefore the width of the vacuum is sufficiently wide, the states (23) are identical to the single slab states (4) over a substantial range of z values (and essentially independent of k_z). In this range, the Fourier coefficients of the expansion (4) are related to their 3D counterparts in (23) by

$$c_{\boldsymbol{k}\alpha}(\boldsymbol{G},z) = \sqrt{\frac{A}{\Omega}} e^{ik_z z} \sum_{G_z} e^{iG_z z} c_{\boldsymbol{k}k_z\alpha}(\boldsymbol{G},G_z). \quad (24)$$

The coefficients f_0 of the asymptotic states (20),(22) can thus be obtained from the supercell states at some suitably chosen transition point z_0 by solution of (17) or, if the coupling of different $c(\boldsymbol{G},z)$ is neglected in favor of computational efficiency, directly from

$$f(\boldsymbol{G},z_0) = \sqrt{\frac{A}{\Omega}} \frac{e^{(\gamma+ik_z)z_0}}{z_0^{u/\gamma}} \sum_{G_z} e^{iG_z z_0} c_{\boldsymbol{k}k_z\alpha}(\boldsymbol{G},G_z). \quad (25)$$

Both approaches allow to extend the Bloch states within a single supercell via

$$\phi_{\boldsymbol{k}\alpha}(\boldsymbol{r}) = \begin{cases} \phi_{\boldsymbol{k}k_z\alpha}(\boldsymbol{r}) & \text{for } 0 \leqslant z \leqslant z_0 \\ \phi_{\boldsymbol{k}\alpha}^{\rm asym}(\boldsymbol{r}) & \text{for } z_0 < z < d/2 \end{cases}, \quad (26)$$

$$\phi_{\boldsymbol{k}\alpha}^{\rm asym}(\boldsymbol{r}) = \frac{e^{i\boldsymbol{k}\cdot\boldsymbol{r}_\parallel}}{\sqrt{A}} \sum_{\boldsymbol{G}} e^{i\boldsymbol{G}\cdot\boldsymbol{r}_\parallel} f(\boldsymbol{G},z) z^{u/\gamma(\boldsymbol{G})} e^{-\gamma(\boldsymbol{G})z}, \quad (27)$$

with f determined by (22) in combination with either (17) or (25). The range $-d/2 < z < 0$ has to be extended analogously. Depending on the symmetry of the slab, the corresponding extension point may have to be chosen different from $-z_0$.

The extension (26) is specified explicitly for the supercell centered at $z = 0$. The states in all other supercells are obtained by periodic repetition (taking care of the phase $e^{ik_z z}$). In practice, only the lowest nonvanishing $\boldsymbol{G}$ need to be included in the expansion (27), since the higher Fourier components decay rapidly due to Eq. (20). Of course, only exponentially decaying states can be extended using (27), i.e., the occupied (and the lowest unoccupied) states.

IV. KLI APPROXIMATION TO THE EXACT EXCHANGE POTENTIAL

The KLI exchange potential [48] consists of two contributions, the Slater term and the orbital-shift term,

$$v_{\text{x}}^{\text{KLI}}(\boldsymbol{r}) = v_{\text{Slater}}(\boldsymbol{r}) + v_{\text{shift}}(\boldsymbol{r}). \tag{28}$$

The Slater term features the exact exchange energy density $e_{\text{x}}(\boldsymbol{r})$,

$$v_{\text{Slater}}(\boldsymbol{r}) = 2 \frac{e_{\text{x}}(\boldsymbol{r})}{n(\boldsymbol{r})}. \tag{29}$$

In the case of spin-saturated slabs, $e_{\text{x}}(\boldsymbol{r})$ and $n(\boldsymbol{r})$ are given by

$$e_{\text{x}}(\boldsymbol{r}) = A \int_{\text{1BZ}} \frac{d^2 k}{(2\pi)^2} \sum_{\alpha} \Theta_{\boldsymbol{k}\alpha} \, e_{\text{x},\boldsymbol{k}\alpha}(\boldsymbol{r}), \tag{30}$$

$$e_{\text{x},\boldsymbol{k}\alpha}(\boldsymbol{r}) = - A \int_{\text{1BZ}} \frac{d^2 k'}{(2\pi)^2} \sum_{\alpha'} \Theta_{\boldsymbol{k}'\alpha'} \int d^3 r'$$

$$\times \frac{\phi_{\boldsymbol{k}\alpha}^{\dagger}(\boldsymbol{r}) \phi_{\boldsymbol{k}'\alpha'}(\boldsymbol{r}) \phi_{\boldsymbol{k}'\alpha'}^{\dagger}(\boldsymbol{r}') \phi_{\boldsymbol{k}\alpha}(\boldsymbol{r}')}{|\boldsymbol{r} - \boldsymbol{r}'|}, \tag{31}$$

$$n(\boldsymbol{r}) = 2A \int_{\text{1BZ}} \frac{d^2 k}{(2\pi)^2} \sum_{\alpha} \Theta_{\boldsymbol{k}\alpha} |\phi_{\boldsymbol{k}\alpha}(\boldsymbol{r})|^2, \tag{32}$$

where $\Theta_{\boldsymbol{k}\alpha}$ denotes the occupation of the state $\boldsymbol{k}\alpha$ and the $\boldsymbol{k}$ integrations extend over the first BZ.

In Ref. [12], it has been demonstrated that v_{Slater} decays as the exact EXX potential,

$$v_{\text{Slater}}(\boldsymbol{r}) \xrightarrow{z \gg L} -\frac{1}{z} + \dots, \tag{33}$$

since the EXX energy density satisfies Eq. (1).

The orbital-shift potential for slabs has the form

$$v_{\text{shift}}(\boldsymbol{r}) = \frac{2A}{n(\boldsymbol{r})} \int_{\text{1BZ}} \frac{d^2 k}{(2\pi)^2} \sum_{\alpha} \Theta_{\boldsymbol{k}\alpha} \Delta_{\boldsymbol{k}\alpha} |\phi_{\boldsymbol{k}\alpha}(\boldsymbol{r})|^2, \tag{34}$$

with

$$\Delta_{\boldsymbol{k}\alpha} = \int_A d^2 r_{\parallel} \int_{-\infty}^{\infty} dz \left[|\phi_{\boldsymbol{k}\alpha}(\boldsymbol{r})|^2 v_{\text{x}}^{\text{KLI}}(\boldsymbol{r}) - e_{\text{x},\boldsymbol{k}\alpha}(\boldsymbol{r}) \right]. \tag{35}$$

The asymptotic behavior of v_{shift} has been investigated in Ref. [56]. To leading order, the asymptotic behavior of both the numerator and the denominator on the right-hand side of Eq. (34) is controlled by the vicinity of the $\boldsymbol{k}$-point(s) for which the exponent $\gamma_{\boldsymbol{k}\alpha}(\boldsymbol{G} = \boldsymbol{0})$ of Eq. (10) assumes its minimum value in the integration region. Depending on the shape of

$\gamma_{\boldsymbol{k}\alpha}(\boldsymbol{G} = \boldsymbol{0})$, one arrives at different results for the individual BZ integrals in Eq. (34). However, proper normalization of the total KS potential, i.e., Eq. (7), requires

$$v_{\text{shift}}(\boldsymbol{r}) \xrightarrow{z \to \infty} 0. \tag{36}$$

This normalization can be ensured by choosing

$$\Delta_{\boldsymbol{q}\alpha} = 0 \tag{37}$$

for the $\boldsymbol{k}$-point(s) $\boldsymbol{q}$ and band(s) α, which yield the lowest value of $\gamma_{\boldsymbol{k}\alpha}(\boldsymbol{G} = \boldsymbol{0})$ under the constraint $\Theta_{\boldsymbol{k}\alpha} > 0$. As a consequence of (37), one obtains

$$v_{\text{shift}}(\boldsymbol{r}) \xrightarrow{z \gg L} \frac{u_{\text{s}}}{z} \tag{38}$$

for many types of band structures [56]. In practice, the asymptotic behavior (38) is assumed only very far outside the surface (compare Ref. [56] and Sec. VIC).

V. COMPUTATIONAL DETAILS: IMPLEMENTATION OF KLI APPROXIMATION FOR SUPERCELL GEOMETRY

In PWPP calculations for slabs on the basis of supercells, the Bloch states are represented by the 3D expansion (23), restricted to the amplitudes with $[\boldsymbol{G}^2 + G_z^2]^{1/2}$ below some 3D cutoff momentum G_{cut},

$$E_{\text{cut}} = \frac{G_{\text{cut}}^2}{2}.$$

Multiplications of and integrations over the states are usually performed by suitably switching from the real-space grid to the finite reciprocal lattice defined by E_{cut} and back via FFTs. If the potential (28) is evaluated in this straightforward manner, the limited cutoff energy of the plane-wave expansion (23) restricts the width of the vacuum: as soon as the states fall below a cutoff-dependent size, their exponential decay (10) can no longer be numerically represented by (23) (compare Fig. 5 of Ref. [12]). This limitation can not be overcome by simply increasing E_{cut}. On the one hand, the computational cost becomes prohibitive with increasing E_{cut}. On the other hand, there is some E_{cut} beyond which the finite numerical representation of numbers limits the accuracy of the leading Fourier amplitudes in (23), so that adding in yet higher amplitudes does no longer improve the result. Thus straightforward EXX-PWPP calculations can not be performed for large vacuum width, even if one utilizes extremely high cutoff energies.

However, at any stage of the evaluation of the KLI potential (28), the 3D real-space states can be extended beyond the stability regime of (23) by use of (26) and (27). This implies that both $e_{\text{x},\boldsymbol{k}\alpha}(\boldsymbol{r})$, Eq. (31), and the numerator of $v_{\text{shift}}(\boldsymbol{r})$, Eq. (34), are evaluated in real space, before they are divided by the real-space density (32). In this way, all components of the KLI potential are numerically well-defined in the middle of the vacuum, even if d becomes large. It turns out that only quite moderate cutoff energies are required to obtain accurate states and thus accurate KLI potentials in the vacuum. In fact, the extension (27) is particularly insensitive to E_{cut}, if only the asymptotically leading term is employed,

$$f(\boldsymbol{G}, z) = f_0(\boldsymbol{G}). \tag{39}$$

A similar insensitivity is found, if the deviation of the asymptotic exchange potential from the leading term is modeled by a δv of the form $-w/z^2$. Compared to the complete neglect of δv, this approach has the advantage that it ensures the continuity of the total potential at the transition point (which is a necessary requirement for obtaining smooth wave functions). In the implementation of this extension scheme, $u = 1$ has been employed, thus simulating the asymptotic behavior of both v_{Slater} and the exact v_{x} of a single slab. δv then accounts for both the deviation of v_{Slater} from $-1/z$ and the complete v_{shift}. In this case, (22) simplifies to[1]

$$f(\boldsymbol{G},z) = f_0(\boldsymbol{G})\left(1 + \frac{\gamma(\boldsymbol{G}) - 1}{2\gamma(\boldsymbol{G})^3 z}\right)\exp\left(-\frac{w}{\gamma(\boldsymbol{G})z}\right), \quad (40)$$

$$w = -z_0\big[z_0\bar{v}_{\mathrm{x}}^{\mathrm{KLI}}(z_0) + 1\big]$$

[$\bar{v}_{\mathrm{x}}^{\mathrm{KLI}}(z)$ denotes the average value of the potential (28) in the 2D unit cell]. The stability of both (39) and (40) stems from the fact that the coefficients f_0 and w are determined completely by the band energies and the potential at the point z_0, but do not require knowledge of δv for $z > z_0$ (compare Sec. VI B).

Use of (22) with the actual δv, on the other hand, requires slightly larger cutoff energies for given z_0 than the simpler approaches (or, alternatively, smaller z_0 for given E_{cut}), since the complete shape of δv enters. Equation (22) can be implemented in two different ways. The first version simulates the correct asymptotics of a single slab potential,

$$f(\boldsymbol{G},z) = f_0(\boldsymbol{G})\left(1 + \frac{\gamma(\boldsymbol{G}) - 1}{2\gamma(\boldsymbol{G})^3 z}\right)\exp\left(-\frac{w}{\gamma(\boldsymbol{G})z}\right)$$

$$\times \exp\left[\frac{1}{\gamma(\boldsymbol{G})}\int_z^{d/2} dz'\,\bar{v}_{\mathrm{shift}}(z')\right], \quad (41)$$

$$w = -z_0[z_0\bar{v}_{\mathrm{Slater}}(z_0) + 1],$$

where $\bar{v}_{\mathrm{shift}}(z)$ and $\bar{v}_{\mathrm{Slater}}(z)$ are the xy averages of the orbital-shift potential (32) and the Slater potential (29), respectively. Equation (41) accounts for the fact that v_{shift} might decay as u_{s}/z in the vacuum, in accordance with Eq. (38). If $\bar{v}_{\mathrm{shift}}(z) = u_{\mathrm{s}}/z$, one has

$$\exp\left[\frac{1}{\gamma}\int_z^{d/2} dz'\,\bar{v}_{\mathrm{shift}}(z')\right] = \left(\frac{d}{2z}\right)^{u_{\mathrm{s}}/\gamma}.$$

This factor restores the additional power-law contribution $z^{-u_{\mathrm{s}}/\gamma}$ required by $\bar{v}_{\mathrm{shift}}(z) = u_{\mathrm{s}}/z$ in the asymptotic solution [$(d/2)^{u_{\mathrm{s}}/\gamma}$ just represents a renormalization of f_0, since d is fixed]. On the other hand, Eq. (41) implies a minor discontinuity in the derivative of the potential, if the actual Slater potential does not behave as $-1/z - w/z^2$ in the transition region.

The second variant accordingly ensures consistence with the true supercell potential,

$$f(\boldsymbol{G},z) = f_0(\boldsymbol{G})\left(1 + \frac{\gamma(\boldsymbol{G}) - 1}{2\gamma(\boldsymbol{G})^3 z}\right)$$

$$\times \exp\left[\frac{1}{\gamma(\boldsymbol{G})}\int_z^{d/2} dz'\left(\bar{v}_{\mathrm{x}}^{\mathrm{KLI}}(z') + \frac{1}{z'}\right)\right]. \quad (42)$$

As a result, this variant is particularly accurate in the transition region. However, this comes at the price that the states do no longer experience a $-1/z$ potential in the middle of the vacuum, where the supercell Slater potential differs from $-1/z$. In this region, one would thus expect the extension (41) to be closer to the single-slab situation than (42). It turns out that the differences between (41) and (42) are quite limited in practice. The more rigorous approaches (41) and (42) are primarily used to verify the accuracy of the simpler schemes.

In principle, the extensions (39)–(42) can be combined with either the solution of (17) or the uncoupled approach (25). In the case of the lowest-order approach (39), however, the inclusion of corrections resulting from coupling would be inconsistent. Equation (39) is therefore always used together with (25). This combination will be called leading-order only (LO) scheme in the following. Similarly, the approximation (40) is always combined with (25), with the intention to establish a computationally efficient and robust, yet reasonably accurate approach. This scheme will be called simple extension (SE). In the case of (41), results from combination with (17), referred to as coupled isolated-slab (CI) scheme, and (25), the uncoupled isolated-slab (UI) scheme, will be compared. Finally, Eq. (42) is always combined with (17). This approach is termed coupled repeated-slab (CR) extension in the following.

Throughout this work, the Monkhorst-Pack scheme [57] is used for $\boldsymbol{k}$-point sampling, with a single sampling point covering the z direction (and without any overall shift, i.e., the offset $\boldsymbol{k}_0$ of Ref. [58] is chosen to be zero). The normalization condition (37) is then implemented for the $\boldsymbol{k}$-point, which yields the lowest exponent $\gamma_{\boldsymbol{k}\alpha}(\boldsymbol{G} = \boldsymbol{0})$ on the discrete Monkhorst-Pack grid (the accuracy of this normalization is discussed in Sec. VI C; $\boldsymbol{k}$-point grids are specified in terms of the Monkhorst-Pack parameters, rather than in terms of the actual number of grid points).

All calculations are based on the experimental lattice constants ($a = 4.65$ Bohr for graphene, $a = 10.26$ Bohr for Si) and the ideal crystal structure. The width of the supercell d is always expressed as a multiple of the lattice constant a. The correlation potential is omitted in all EXX/KLI calculations, in order to extract the behavior of the EXX/KLI potential as cleanly as possible.

VI. RESULTS

A. Extension of Bloch states

The obvious first question to be addressed is the accuracy of the extension (27) of the Bloch states and, in particular, the dependence of this scheme on the transition point z_0. As discussed in detail in Ref. [12], there is an intermediate range of z values for which the states and potentials of supercell calculations are close to the corresponding quantities of a single slab. Consequently, z_0 must neither be too small (otherwise the asymptotic form of the states has not yet been reached) nor too large, since in the middle of the vacuum between two neighboring slabs the states (23) no longer experience a KS potential decaying like $1/z$. In addition, the magnitude of the states at z_0 has to be sufficiently far above the numerical noise level to ensure an accurate evaluation of the G_z sum in (24).
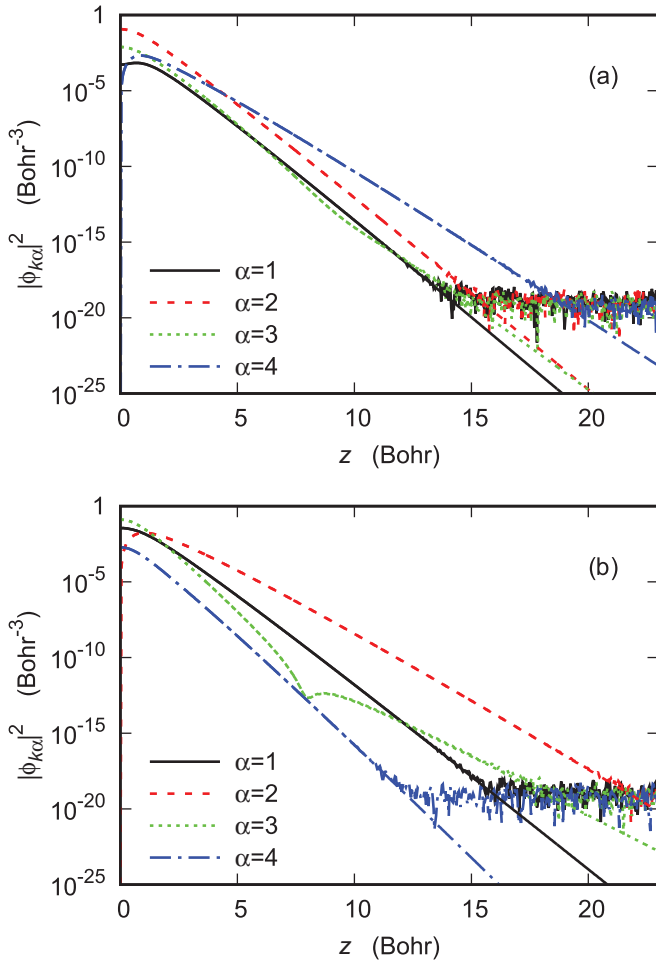
---

[1]If $w \ll \gamma z$ the exponential function can, of course, be expanded, $\left(1 + \frac{\gamma-1}{2\gamma^3 z}\right)\exp\left(-\frac{w}{\gamma z}\right) \approx \left(1 + \frac{\gamma-1}{2\gamma^3 z} - \frac{w}{\gamma z}\right)$.
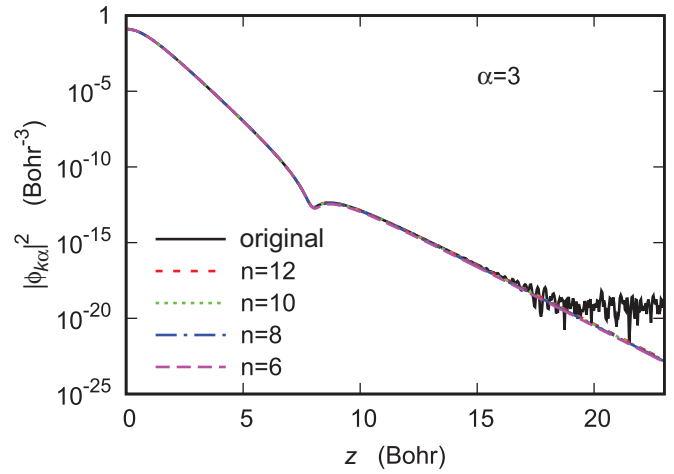
FIG. 2. Density $|\phi_{k\alpha}(r)|^2$ of state $\alpha = 3$ at $k = k_b$, Eq. (46), for different transition points from the numerical Fourier expanded state (23) to the analytical asymptotic form (27), using the SE scheme: comparison of transition points 4.02, 5.42, 6.89, and 9.04 Bohr resulting from $s = 10^{-n}$ Bohr^{-3} with $n = 6$, 8, 10, and 12, respectively (x, y, d, and E_{cut} as in Fig. 1).

figure caption, all computational details are as in Ref. [12]; the corresponding information on a 6-layer Si(111) slab is given in Appendix A). In the case of Fig. 1(a), the transition points are 6.46, 6.46, 5.92, and 8.72 Bohr for $\alpha = 1$, 2, 3, and 4, respectively; for Fig. 1(b), the corresponding z_0 are 6.82, 9.51, 5.42, and 5.31 Bohr. As both figures demonstrate, the extensions are indistinguishable from the original states over a substantial range of z values. Differences only set in when the original states reach the noise floor.

This observation is confirmed by variation of the transition point. A particularly illustrative case to consider is the state $\alpha = 3$ at $k = k_b$ [see Fig. 1(b)]. The Fourier representation (27) of this state is dominated by the components of the lowest nonvanishing G-vectors. For small z, this state therefore decays much more rapidly than the more deeply bound states $\alpha = 1$ and 2, for which the Fourier component with $G = 0$ dominates. However, $c_{k\alpha}(G = 0, z)$ is nonzero also for the state $\alpha = 3$, which becomes visible beyond $z = 8$ Bohr and ultimately lets this state decay more slowly than the lower-lying states. By contrast, $c_{k\alpha}(G = 0, z)$ vanishes completely for the highest occupied state ($\alpha = 4$), which therefore decays faster than all others (at this k-point).

Figure 2 provides the variation of the SE result for the most critical state with the transition point. Four different density thresholds (10^{-n} Bohr^{-3} with $n = 6, 8, 10, 12$) are compared. On the logarithmic scale of the figure the four variants are essentially indistinguishable, which is quite remarkable in view of the transition point $z_0 = 4.02$ Bohr for the highest s.

Given the agreement observed, it is obvious that the more accurate extension schemes cannot be distinguished from the SE approach on plots such as Figs. 1 and 2. A more sensitive quantity for an analysis of the continuity of the states at the transition point and the dependence of the extension on z_0 is the logarithmic derivative

$$\frac{\partial}{\partial_z} \ln[|\phi_{k\alpha}(r)|^2] = \frac{\partial_z |\phi_{k\alpha}(r)|^2}{|\phi_{k\alpha}(r)|^2}. \tag{47}$$

FIG. 1. Densities $|\phi_{k\alpha}(r)|^2$ of occupied states of graphene as functions of z for $x = \frac{9a}{128}$ and $y = \frac{\sqrt{3}a}{32}$: (a) $k = k_a$, Eq. (45); (b) $k = k_b$, Eq. (46). Both the original numerical state (23) and its extension by the SE approach are shown. z_0 is defined by (44) with $s = 10^{-8}$ Bohr^{-3} ($d = 10a \approx 46.5$ Bohr, $E_{cut} = 1880$ Ry).

An appropriate means for handling the transition point z_0 is the average density of a Bloch state for given z,

$$n_{k\alpha}(z) = \frac{1}{A} \int_A d^2 r_\| \, |\phi_{k\alpha}(r)|^2, \tag{43}$$

i.e., z_0 is determined by the (outermost) point for which $n_{k\alpha}(z)$ falls below a predefined threshold s,

$$z_0 = \max \{z | n_{k\alpha}(z) \geqslant s\}. \tag{44}$$

Figure 1 shows the occupied states of graphene for two prototype k-points,

$$k_a = \frac{2\pi}{a} \left(-\frac{1}{8}, -\frac{1}{\sqrt{3}} \right), \tag{45}$$

$$k_b = \frac{2\pi}{a} \left(0, -\frac{1}{8\sqrt{3}} \right). \tag{46}$$

For each state, the original numerical result (23), visible by the fact that its decay is limited by the numerical noise level, is compared to the extension (27), with $f(G, z)$ resulting from the SE scheme and $s = 10^{-8}$ Bohr^{-3} (for further details see
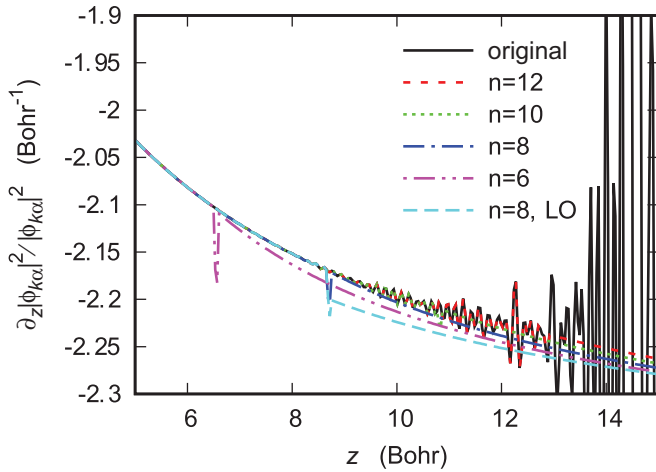
FIG. 3. Logarithmic derivative (47) of state $\alpha = 4$ at $\boldsymbol{k} = \boldsymbol{k}_a$, Eq. (45), for different transition points from the numerical Fourier expansion (23) to the analytical asymptotic form (27), using the SE scheme: comparison of transition points 6.57, 8.72, 10.84, and 12.88 Bohr resulting from $s = 10^{-n}$ Bohr^{-3} with $n = 6$, 8, 10, and 12, respectively (x, y, d, and E_{cut} as in Fig. 1). Also shown is the LO extension for $s = 10^{-8}$ Bohr^{-3}.

Figure 3 shows this quantity for the highest occupied state of Fig. 1(a). Figure 3 confirms that the SE approach ensures almost continuous first logarithmic derivatives of the states. Only a tiny spike right at the transition point indicates the extension. This spike is primarily due to the truncation of the expansion (27): only the star of the smallest nonvanishing $\boldsymbol{G}$-vectors is included in the extensions for all figures of this section (with the exception of Fig. 4). The neglect of all higher $\boldsymbol{G}$ introduces a minor discontinuity in the wave function, too small to be visible in Fig. 1. Due to its origin, the magnitude of the spike in the logarithmic derivative reduces substantially with increasing z_0, suggesting to avoid thresholds higher than 10^{-8} Bohr^{-3}. Alternatively, one can improve continuity by including larger $\boldsymbol{G}$-vectors in (27), as demonstrated below in Fig. 4. It seems worthwhile to remark that even $\partial_z^2|\phi_{k\alpha}(\boldsymbol{r})|^2/|\phi_{k\alpha}(\boldsymbol{r})|^2$ is more or less continuous in the transition region, again with the exception of a spike at z_0. As a result, the derivative of (27) remains almost identical with the derivative of the original state until numerical noise starts to dominate the latter quantity. It is thus no surprise that little deviation is found for different transition thresholds.

In addition to SE results, Fig. 3 also provides the wave function obtained with the LO scheme. The neglect of any correction for the difference between the asymptotic EXX/KLI potential and $-1/z$ leads to a discontinuous derivative at the transition point. However, ultimately the LO and SE wave functions converge to the same asymptotic limit, so that the simplest form re-approaches the continuous extension with increasing z.

In order to examine the continuity of the states and their derivatives in yet more detail, one has to display the ratio between the extension (27) and the original numerical wave function right after the transition point. Figure 4(a) shows this ratio for the LO, SE, and UI extensions relying on the uncoupled matching (25). If only the star of the lowest non-
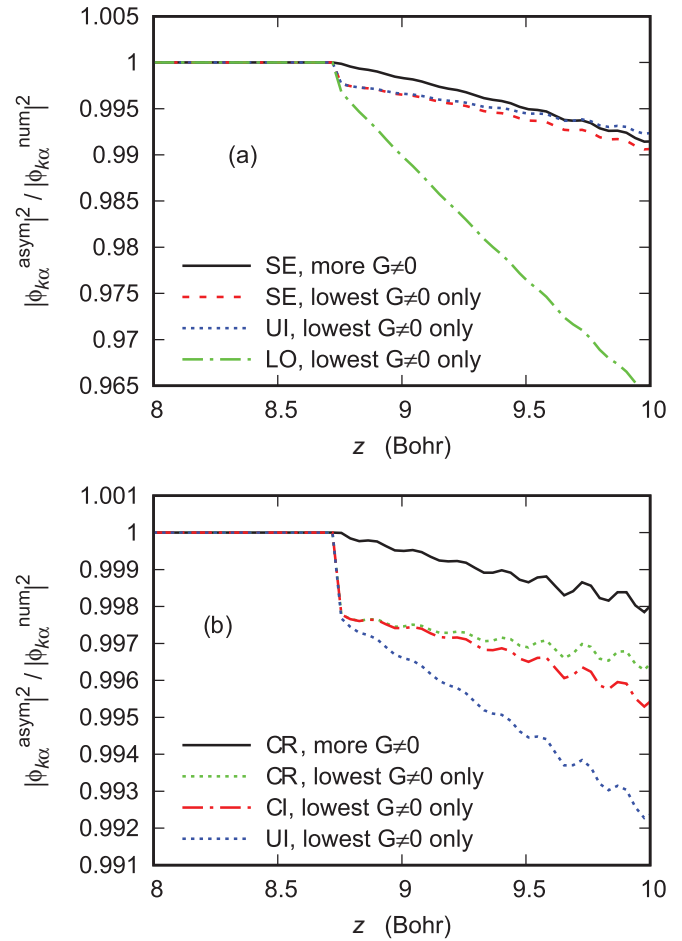

FIG. 4. Ratio of extension (27) to numerical wave function (23) in the vicinity of the transition point for Bloch state $\alpha = 4$ at $\boldsymbol{k} = \boldsymbol{k}_a$, Eq. (45): (a) LO, SE, and UI extensions including only the star of the lowest nonvanishing $\boldsymbol{G}$-vectors vs SE including the stars of the four lowest $\boldsymbol{G} \neq \boldsymbol{0}$; (b) UI versus CI and CR extensions for differently many $\boldsymbol{G} \neq \boldsymbol{0}$ ($z_0 = 8.72$ Bohr, x, y, d, and E_{cut} as in Fig. 1).

vanishing $\boldsymbol{G}$ is included in (27), the absolute value of the wave function drops by 0.25% at z_0 (for the present choice of s), irrespective of whether the deviation of the potential from $-1/z$ is simulated by the SE form (40) or the UI variant (41). In both cases, continuity of the states can be ensured by inclusion of the four lowest stars of nonvanishing $\boldsymbol{G}$. However, this continuous extension soon approaches the restricted one, since the additional components decay faster than the leading terms. As a result, the neglect of higher $\boldsymbol{G} \neq \boldsymbol{0}$ leads to inaccuracies only close to the transition point.

Figure 4(a) reveals that a minor discontinuity remains in the derivative of the states, even if higher $\boldsymbol{G}$-vectors are included. Moreover, the relevance of the higher $\boldsymbol{G}$-vectors for the continuity of the states points at the importance of the coupling of different amplitudes via $v(\boldsymbol{G} - \boldsymbol{G}', z)$. Figure 4(b) correspondingly provides results obtained with the coupled scheme (17). Irrespective of whether the single-slab simulation CI or the supercell implementation CR is used, only a tiny discontinuity in the derivative is left. The reason for the particular importance of coupling is that the state considered in Figs. 3 and 4 corresponds to a $\boldsymbol{k}$-point on the boundary of
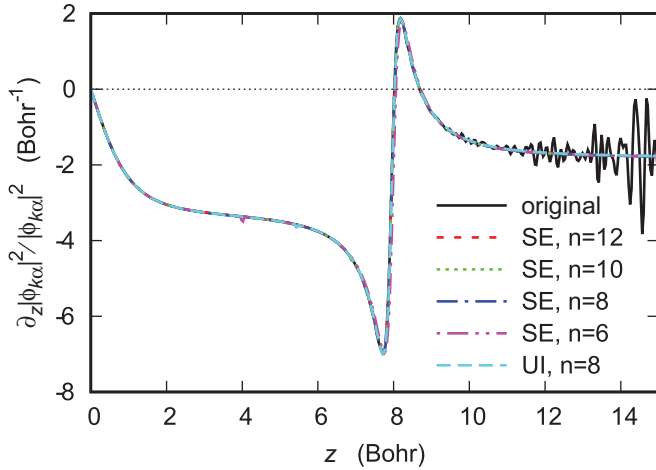
FIG. 5. Logarithmic derivative (47) of state $\alpha = 3$ at $\boldsymbol{k} = \boldsymbol{k}_b$, Eq. (46) for different transition points from the numerical Fourier expansion (23) to the analytical asymptotic wave function (27) obtained with the SE scheme: comparison of transition points 4.02, 5.42, 6.89, and 9.04 Bohr resulting from $s = 10^{-n}$ Bohr^{-3} with $n = 6$, 8, 10, and 12, respectively (x, y, d, and E_{cut} as in Fig. 1). Also shown is the UI scheme for $s = 10^{-8}$ Bohr^{-3}.

the first BZ: the difference between the SE/UI schemes and the CI/CR variants primarily originates from the coupling of $c(\boldsymbol{0}, z)$ to the single amplitude $c(\boldsymbol{G} \neq \boldsymbol{0}, z)$ with $\gamma(\boldsymbol{G}) = \gamma(\boldsymbol{0})$. One should note, however, that (i) the states on the boundary of the first BZ are usually irrelevant for the asymptotics of the potential (which is controlled by the most weakly decaying states [56]), and (ii) the discontinuity of the SE derivative is still of the same order of magnitude as that resulting from the more advanced schemes.

Finally, Fig. 5 displays the logarithmic derivative of the state considered in Fig. 2, for which $\boldsymbol{k}$ is close to the Γ-point. Again, one observes an accurate reproduction of the original state (wherever this state is meaningful) and invariance against variation of z_0. We just remark that the more advanced CI and CR extensions can not be distinguished from the results of the SE and UI approaches on the scale of Fig. 5.

To summarize, depending on the degree of continuity desired and the transition threshold chosen, no more than a few of the lowest nonvanishing $\boldsymbol{G}$ have to be included in the extension (27). If only the lowest $\boldsymbol{G} \neq \boldsymbol{0}$ is used, a minor discontinuity of the state has to be accepted for the computationally more attractive higher thresholds. This discontinuity leads to a small spike in the derivative of the state. If one sets this spike aside, the continuity of the derivative depends on the level of the extension scheme. While complete continuity for all kinds of states can be ensured by use of the CI and CR schemes, the technically much simpler SE approach also leads to reasonably continuous derivatives, in particular for states deep inside the first BZ.

B. Extension of KLI exchange potential

The limited sensitivity of the states to the choice of both the transition point and the extension scheme translates into a similarly limited sensitivity of the KLI exchange potential. In fact, the KLI potential is even somewhat less critical,
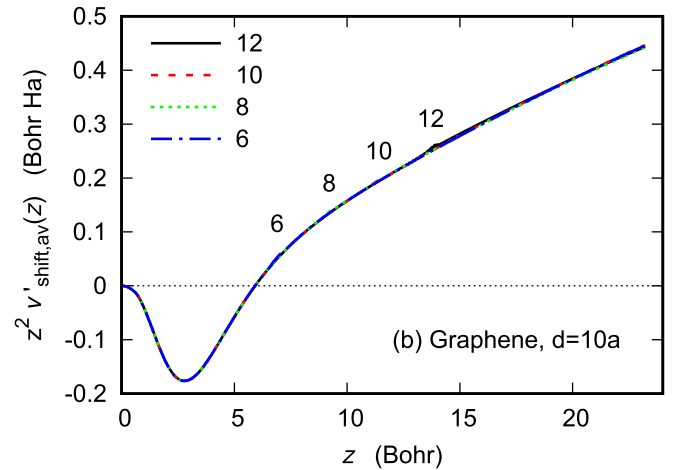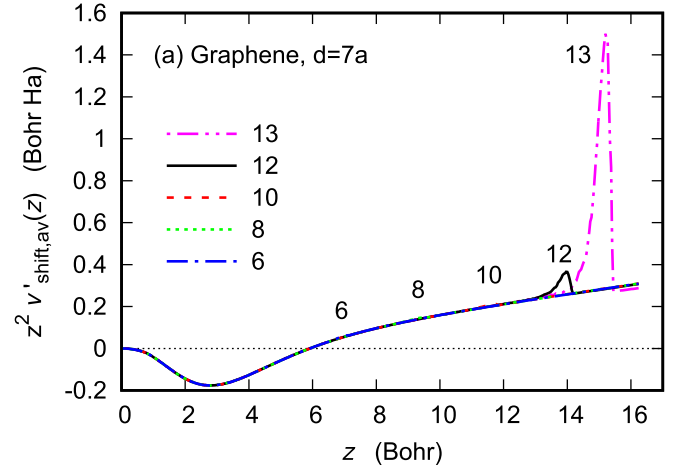

FIG. 6. Derivative of x-y-averaged v_{shift}, Eq. (34), for graphene: comparison of different transition points, resulting from UI scheme and density thresholds $s = 10^{-n}$ Bohr^{-3}. (a) vacuum width $d = 7a$, $n = 6$–13; (b) vacuum width $d = 10a$, $n = 6$–12. The position of the number indicates the associated transition point ($E_{cut} = 1880$ Ry, 8×8 $\boldsymbol{k}$-point grid).

since inaccuracies in the numerator of v_x^{KLI}, resulting from the extension of the states, are partially compensated by the corresponding inaccuracies in the denominator. It turns out that the orbital-shift term (34) varies slightly more with both z_0 and the form of $f(\boldsymbol{G}, z)$ than v_{Slater}, so that the discussion will focus on v_{shift} in the following.

Figure 6 shows the first derivative of v_{shift} for graphene, averaged over x and y, i.e., the $\boldsymbol{G} = \boldsymbol{0}$ Fourier component. As in the case of the states, the derivative $\partial_z v_{shift}$ reveals any discontinuity more clearly than the potential itself. Different transition thresholds and two different vacuum widths are compared on the basis of the UI scheme. Focusing first on Fig. 6(a) (where $d = 7a$), one observes that $\partial_z v_{shift}$ is independent of z_0 for all density thresholds above 10^{-12} Bohr^{-3}. Starting with $s = 10^{-12}$ Bohr^{-3}, one finds an obvious discontinuity in $\partial_z v_{shift}$, which becomes quite large for $s = 10^{-13}$ Bohr^{-3}. However, this is exactly the expected behavior: if the transition points of the most weakly decaying states approach the middle of the vacuum, a continuous extension of the states via Eq. (27) is no longer possible. The discontinuity of $\partial_z v_{shift}$ just signifies

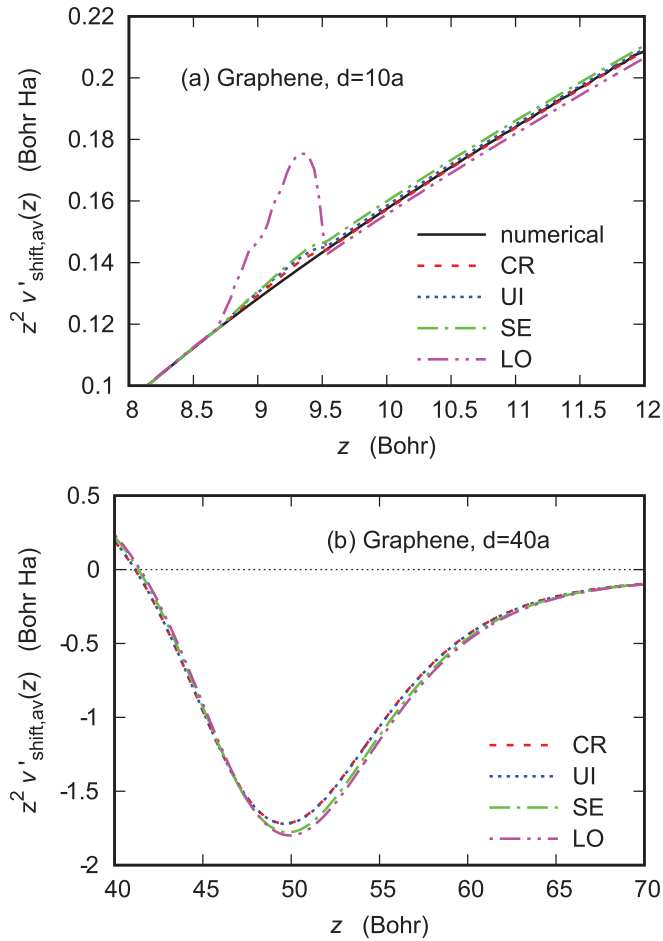FIG. 7. Derivative of x-y-averaged v_{shift}, Eq. (34), for graphene: comparison of different extension schemes for (a) the transition region ($d = 10a$, $E_{cut} = 1880$ Ry) and (b) very large z ($d = 40a$, $E_{cut} = 520$ Ry) (in all cases $s = 10^{-8}$ Bohr^{-3}, 8×8 $\boldsymbol{k}$-point grid).

that the threshold is too low for the vacuum width under consideration. Note, however, that Fig. 6 displays $z^2 \partial_z v_{shift}$, which emphasizes differences for large z.

This interpretation is confirmed by Fig. 6(b) where d was chosen to be $10a$, just as in Figs. 1–5. Now a threshold of 10^{-12} Bohr^{-3} is unproblematic. Of course, a low threshold requires a high cutoff energy, so that a less ambitious s is still preferable.

Figure 7(a) shows the transition region on an enlarged scale. The SE approach is compared to the UI and LO schemes, which are also based on the uncoupled solution (25), as well as to the more advanced CR scheme (the results of the CI approach can not be distinguished from the UI data in all figures of this section and are therefore suppressed). Figure 7(a) demonstrates that the simple extension is very close to the more rigorous approaches. On the other hand, the complete neglect of any correction to the leading order leads to an obvious peak in $\partial_z v_{shift}$. However, even the LO extension is close to the true result once the transition region is passed (note that the plot shows $z^2 \partial_z v_{shift}$).

Figure 7(b) provides a corresponding comparison for very large z. Clearly, the structure of $\partial_z v_{shift}$ resulting from the different schemes is very similar, in spite of the fact that the
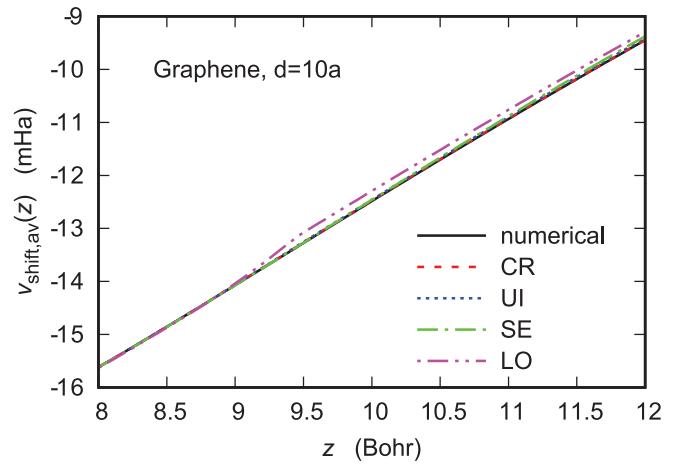

FIG. 8. x-y-averaged v_{shift}, Eq. (34), for graphene: comparison of different extension schemes ($s = 10^{-8}$ Bohr^{-3}, $E_{cut} = 1880$ Ry, 8×8 $\boldsymbol{k}$-point grid).

function (40) rapidly approaches a constant with increasing z, while the inclusion of the actual asymptotic potential in the functions (41) and (42) leads to some variation of $f(\boldsymbol{G}, z)$ also for large z. In fact, in the range considered, even the LO extension is quite close to the correct result. Figure 7(b) also demonstrates that the coupling of the $c(\boldsymbol{G}, z)$ via (17) is of minor importance in the truly asymptotic region: the potentials resulting from the UI, CI, and CR schemes are on top of each other. For large z, the amplitude $c(\boldsymbol{0}, z)$ dominates over all others for the most weakly decaying states in the vicinity of the Γ-point [56]. The small differences observed in Fig. 7(b) solely originate from the rigorous treatment of v_{shift} in the UI, CI, and CR schemes.

The potentials corresponding to the derivatives in Fig. 6 can not be distinguished, with the exception of the most extreme case ($d = 7a$ with $s = 10^{-13}$ Bohr^{-3}). The maximum deviation between the v_{shift} obtained for the different thresholds is of the order of 0.1 mHa in the case of Fig. 6(b). The largest deviation is always found close to the transition point of the most weakly decaying state. Similarly, the differences between the SE potentials and the results of the more accurate UI, CI, and CR schemes are no larger than 0.1 mHa (compare Fig. 8). Even the extension via only the leading order deviates from the other schemes by less than 0.2 mHa. This error is accumulated in the transition region and does not increase with z.

The variation of $\partial_z v_{Slater}$ with the transition threshold and the extension scheme can not be resolved on the scale used for Fig. 6, even the second derivative of v_{Slater} is almost continuous. As a result, the differences between the Slater potentials from different s are below 10 μHa even in the case of the SE approach.

Moreover, the normalization of the KLI potential is controlled by Eq. (37). The value of $\Delta_{\boldsymbol{q}\alpha}$, however, is essentially independent of the form of v_x^{KLI} in the extreme asymptotic region in which the states are extended via (27). As a result, the normalization of the potential and therefore all band energies are highly independent of the extension scheme used: for instance, the Fermi energy resulting from the SE approach differs by less than 10^{-7} Ha from the result of the CR extension.

TABLE I. Fermi energy of 6-layer Si(111) slab: EXX-only (in KLI approximation) results as a function of the width of the vacuum $\bar{d}$ and k-point sampling (all energies in mHA). The last digit is only given to demonstrate the convergence, but does not reflect the absolute accuracy of the data.

$\bar{d}$	k-point sampling		
$(a/\sqrt{3})$	8×8	16×16	32×32
4	248.33		
6	247.93	247.08	
8	247.81	247.05	246.94
10	247.75	247.04	246.94
20	247.58	247.01	246.93
40	247.49	246.99	246.93
80	247.43	246.98	246.93

For that reason all results for graphene in Secs. VIC–VIE have been obtained with the SE scheme (with the exception of Fig. 16).

Appendix A provides the counterparts of Figs. 7 and 8 for a 6-layer Si(111) slab. The variation of the asymptotic exchange potential with the extension scheme is clearly larger than observed for graphene, the reason being the less pronounced minimum of the exponent $\gamma_{k\alpha}(\boldsymbol{G} = \boldsymbol{0})$ at the Γ-point (compare Ref. [56]). In the case of very wide vacua, the deviation between the various approaches becomes as large as 4 mHa in the region about 100 Bohr outside the surface, if a high-resolution $\boldsymbol{k}$-point grid is employed. At the same time, the Fermi energies resulting from the different schemes agree within 1 μHa in the case of highly converged calculations. For that reason all Fermi energies for Si(111) slabs reported in Table I are based on the particularly efficient LO extension. On the other hand, the data in Table II and the asymptotic potentials in Fig. 17 were obtained with the CI approach.

The independence of the results from both z_0 and the extension scheme even holds for extreme extrapolations, the reason being that the ultimate asymptotic form (10) of the states only depends on their eigenvalues, for which the proper normalization of the potential is relevant, but not its precise asymptotic decay. At the same time, the extension does not require very high cutoff energies. Both properties are demonstrated in Fig. 9 for a particularly challenging situation, a 6-layer Si(111) slab

TABLE II. Work function of graphene as well as Si(111) slabs (without relaxation): EXX-only (in KLI approximation) vs LDA (with VWN correlation [63]) and PBEsol-GGA [64] results with and without correlation. The experimental values for graphene [65] and bulk Si are also listed (all energies in eV).

method	graphene	Si(111)		
		6 layers	12 layers	18 layers
Expt.	4.6			(4.60)
LDA/VWN	4.55	5.05	4.89	4.91
PBEsol	4.23	4.68	4.54	4.56
LDA x-only	3.21	3.99	3.81	3.82
PBEsol x-only	2.89	3.66	3.51	3.52
EXX-only/KLI	8.57	6.72	6.52	6.53
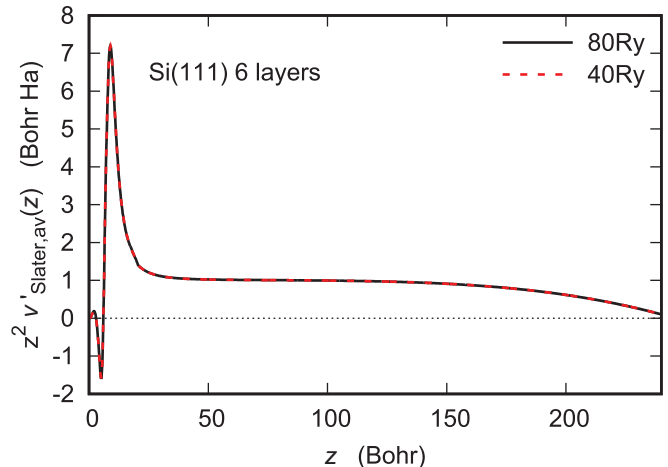
FIG. 9. First derivative of x-y-averaged v_{Slater}, Eq. (29), for a 6-layer Si(111) slab with $d = 82a/\sqrt{3}$ (32×32 $\boldsymbol{k}$-point grid, LO extension).

with the exceptional vacuum width of 480 Bohr. In analogy to Fig. 6 the derivative of v_{Slater} is plotted, which exhibits numerical noise and lack of convergence more clearly than the potential itself. Figure 9 shows that the derivative of v_{Slater} is fully converged for an E_{cut} of 40 Ry.

A similar insensitivity is observed for v_{shift} and in the case of other slabs. In fact, if an E_{cut} of only 60 Ry is used for the calculations underlying Figs. 10 and 11, the resulting v_{Slater} is indistinguishable from the data plotted (provided that the transition threshold controlling z_0 is reduced accordingly). Essentially the same applies to the derivative of v_{Slater}, only in the transition region for the various states differences of 1%–2% are observed, depending on the particular choice for the threshold. Even for moderate cutoff energies and very wide vacua, the potentials resulting from the extension procedure are numerically stable and accurate. Many figures of this contribution, in particular Figs. 6–8, nevertheless rely on a rather high E_{cut} in order to allow use of very low density thresholds for the transition point and to extract even minor inaccuracies.

C. KLI exchange potential: k-point convergence

Before a discussion of the asymptotic form of the EXX/KLI potential, the convergence of $v_{\text{x}}^{\text{KLI}}$ with the number of $\boldsymbol{k}$-points has to be addressed. It is instructive to analyze the components (29) and (34) separately. We start with v_{Slater}, using again graphene as a prototype example. As is well known, application of the EXX to metals requires notoriously many $\boldsymbol{k}$-points to integrate over the BZ, so that the presence of the Dirac points for graphene indicates that some care might be necessary. Figure 10 shows the dependence of v_{Slater} on the $\boldsymbol{k}$-point sampling for a vacuum width of $d = 10a$. Both v_{Slater} itself and its derivative with respect to z are shown. The scaled derivative $z^2 \partial_z v(z)$ is a particularly sensitive quantity, which allows to extract the deviation of $v(z)$ from $-1/z$ most clearly, and is therefore included in all subsequent figures. The results of the $\boldsymbol{k}$-point sampling with a 24×24 Monkhorst-Pack grid are
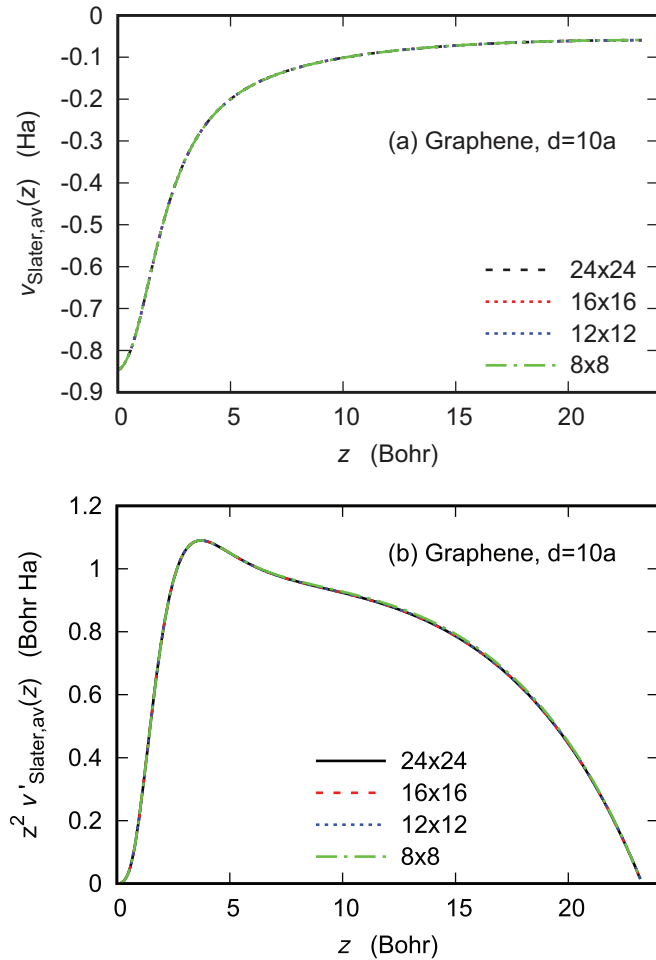
FIG. 10. Convergence of (a) x-y-averaged v_{Slater}, Eq. (29), and (b) its first derivative with respect to z with $\boldsymbol{k}$-point sampling. The $\boldsymbol{k}$-point grids used are characterized by the Monkhorst-Pack parameters [57] ($d = 10a = 46.5$ Bohr, $E_{\text{cut}} = 520$ Ry, SE scheme).
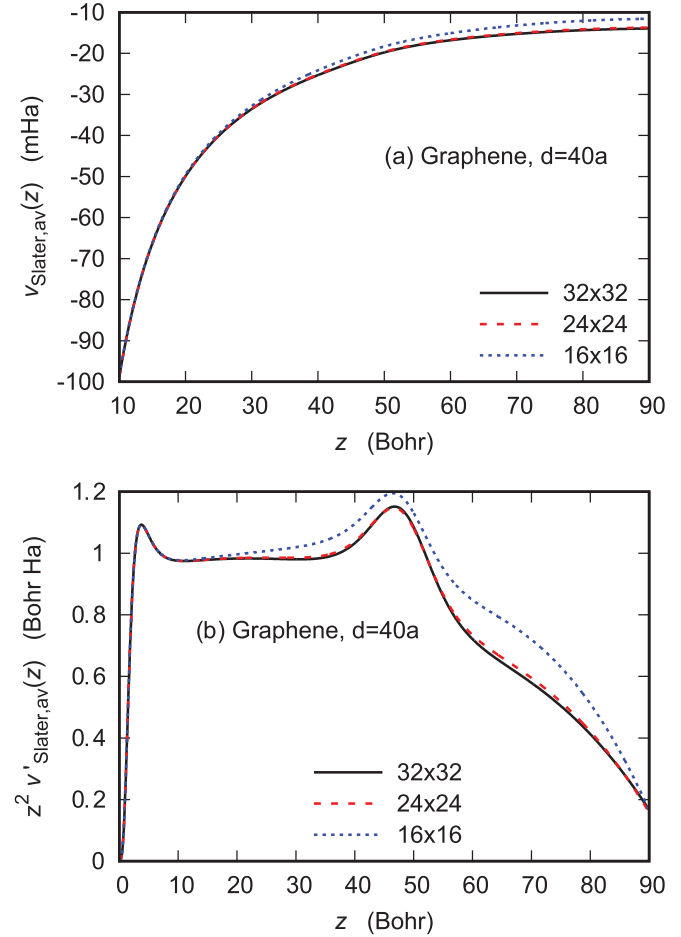
FIG. 11. As Fig. 10 for $d = 40a = 186$ Bohr. For $z < 10$ Bohr, the potentials of panel (a) can not be distinguished from the corresponding results in Fig. 10(a).

indistinguishable from those obtained with the much coarser 8×8 grid.

The situation is, however, different for wider vacua, as illustrated in Fig. 11. It needs at least a 24×24 grid to obtain converged results for $d = 40a$. The reason for this sensitivity is the unsophisticated handling of the EXX Coulomb singularity in the present work, which follows the scheme introduced in Ref. [59] (with a correction term[2]). As soon as the cells in the BZ covered by a single sampling point become too flat (due to large d), the discrete sampling of the BZ starts to fail. It remains to be seen whether any of the more advanced approaches for handling the Coulomb singularity in the exact exchange [27,28,36,60] improves the convergence.

Turning to v_{shift}, Eq. (34), the convergence with the $\boldsymbol{k}$-point grid is investigated in Figs. 12 and 13 for $d = 10a$ and $d = 40a$, respectively. For both d, the derivatives of v_{shift} obtained from

different $\boldsymbol{k}$-point grids are almost identical (with the exception of the very coarse 8×8 sampling for $d = 40a$), so that the corresponding potentials can only differ by some constants. Convergence of the normalization of v_{shift}, however, requires a quite dense $\boldsymbol{k}$-point sampling: the accuracy of the overall normalization depends on how close the discrete $\boldsymbol{k}$-point grid comes to the point $\boldsymbol{k} = \boldsymbol{q}$ at which $\gamma_{\boldsymbol{k}\alpha}(\boldsymbol{G} = \boldsymbol{0})$ has its minimum (for graphene this is the Γ-point). It needs at least a 24×24 Monkhorst-Pack grid to obtain fully converged results, irrespectively of the value of d. Convergence can be improved by shifting the standard Monkhorst-Pack grid such that one of its $\boldsymbol{k}$-points agrees with $\boldsymbol{q}$ (which has not been done in this work). One has to emphasize, however, that even the 8×8 grid leads to an error in normalization of no more than 2 mHa.

D. KLI exchange potential: asymptotic form

On this basis one can now examine the asymptotic behavior of the KLI exchange potential. Its Slater component shows exactly the expected shape in the vacuum [12]: it is close to $-1/z$ in the range $L \ll z \ll d/2$ and bends around when z approaches $d/2$ (see Figs. 9–11). The convergence of v_{Slater} against $-1/z$ with increasing d is displayed in Fig. 14, once
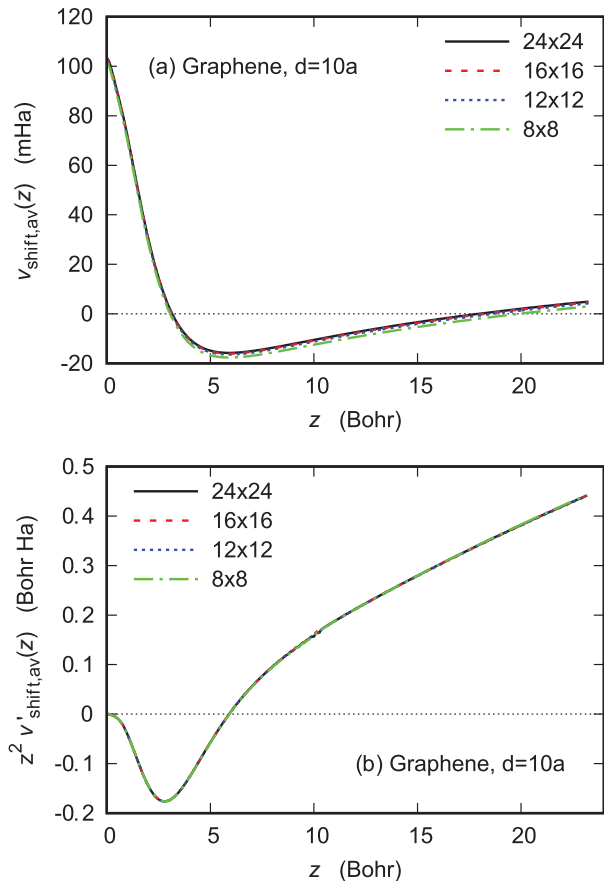
---

[2]The correction term for the Coulomb singularity is a reduced version of the correction introduced in Ref. [78]: only the major contribution to the Duchemin and Gygi correction is included, which can be done at absolutely no computational cost.

FIG. 12. Convergence of (a) x-y-averaged v_{shift}, Eq. (34), and (b) its first derivative with respect to z with $\boldsymbol{k}$-point sampling. The $\boldsymbol{k}$-point grids used are characterized by the Monkhorst-Pack parameters [57] ($d = 10a = 46.5$ Bohr, $E_{cut} = 520$ Ry, SE scheme).
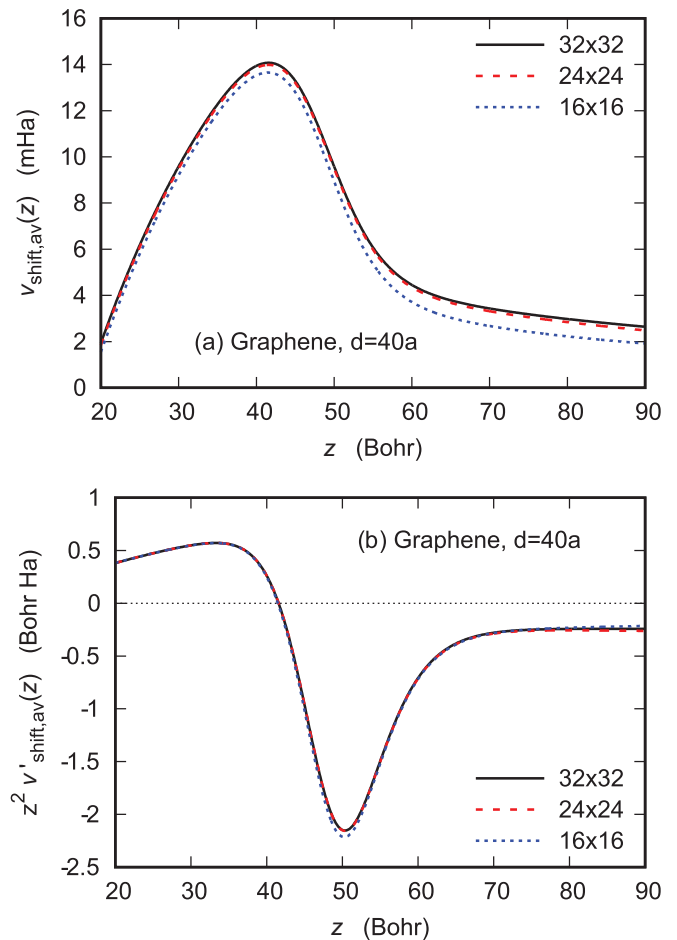

FIG. 13. As Fig. 12 for $d = 40a = 186$ Bohr. For $z < 20$ Bohr, both the potentials and their derivatives can not be distinguished from the corresponding results in Fig. 12.

more for graphene. The potential from $d = 40a$ can not be distinguished from $-1/z$ on the scale of Fig. 14(a).

The stability of v_{shift} under variation of d is already indicated in Figs. 12 and 13. Figure 15 explicitly confirms this invariance. Neither the potentials from different d nor their derivatives can be distinguished, the normalization of v_{shift} is independent of d. However, these figures also show that v_{shift} remains sizable for rather large z, quite different from its rapid decay in the asymptotic region of atoms. On the one hand, one observes a peak around 40 Bohr, whose amplitude of 14 mHa is of the same order of magnitude as the 25 mHa depth of the Slater potential. On the other hand, Fig. 13(b) illustrates the z^{-1} dependence of v_{shift} for very large z, predicted by the analytical result (38) [Fig. 13(b) indicates that $u_s \approx 1/4$ for graphene].

An early decay of v_{shift} is prevented by the fact that the most weakly decaying states dominate the density only for very large z. This is obvious from Fig. 1(b), which shows the most weakly decaying state[3] for the case of the 8×8 $\boldsymbol{k}$-point grid: the state $\alpha = 3$ at $\boldsymbol{k} = \boldsymbol{k}_b$ ultimately vanishes more slowly than all other states, as it has the lowest $\gamma_{\boldsymbol{k}\alpha}$ of all occupied states with $f_{0,\boldsymbol{k}\alpha}(\boldsymbol{G} = \boldsymbol{0}) \neq 0$ (on the 8×8 grid).

---

[3]Of course, this state stands as representative of the complete set of states at equivalent $\boldsymbol{k}$-points.

Its amplitude $f_{0,\boldsymbol{k}\alpha}(\boldsymbol{G} = \boldsymbol{0})$ is, however, quite small, so that this state starts to dominate the complete density no earlier than beyond 50 Bohr. Since v_{shift} is the ratio of a sum over the Bloch state densities with weights given by $\Delta_{\boldsymbol{k}\alpha}$ and the density itself, v_{shift} is bound to exhibit some structure until finally the asymptotically dominating states control both the numerator and the denominator. Unlike assumed in Ref. [12], there is a mechanism which introduces a length scale into the KLI exchange potential much larger than a.

The small amplitude $f_{0,\boldsymbol{k}\alpha}(\boldsymbol{G} = \boldsymbol{0})$ of the most weakly decaying state is a manifestation of the fact that one has $f_{0,\boldsymbol{k}\alpha}(\boldsymbol{G} = \boldsymbol{0}) = 0$ for the two degenerate highest occupied states at the Γ-point, for which $\gamma_{\boldsymbol{k}\alpha}$ assumes its minimum value in the BZ (see Fig. 1 of Ref. [56]). The amplitude $f_{0,\boldsymbol{k}\alpha}(\boldsymbol{G} = \boldsymbol{0})$ builds up only slowly, when one leaves the Γ-point. As a result, the asymptotic behavior is approached particularly slowly in both the numerator and the denominator of (34).

Taking Figs. 14 and 15 together then shows that the complete EXX/KLI potential inside the slab and in the surface region is invariant under variation of d. In fact, the well depth is converged already for quite moderate vacua.

Figure 16 finally compares the total EXX/KLI potential of graphene with $-1/z$. The deviation of v_x^{KLI} from $-1/z$ in the region around 40 Bohr, resulting from the long-range
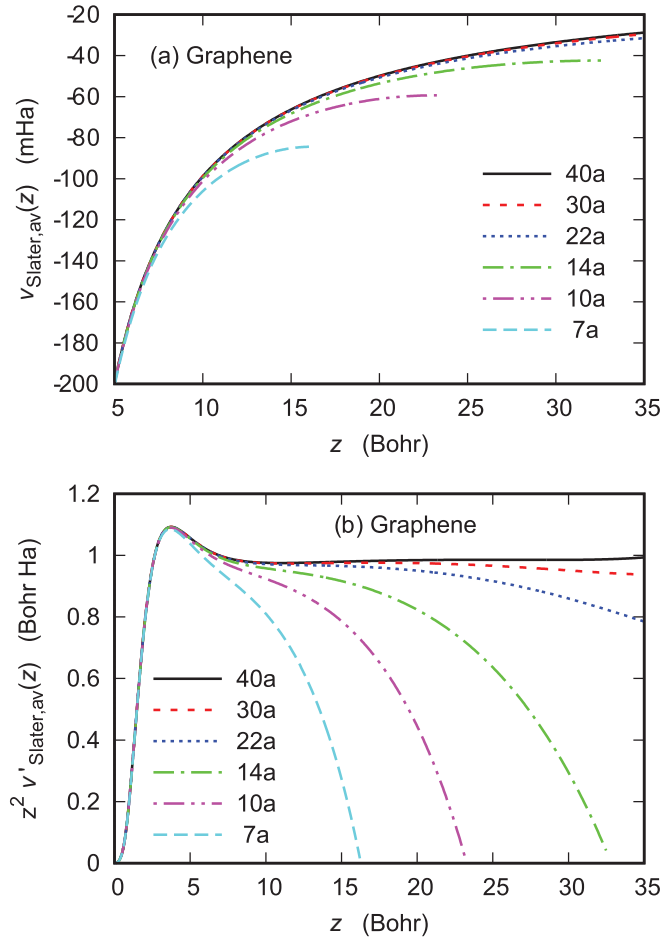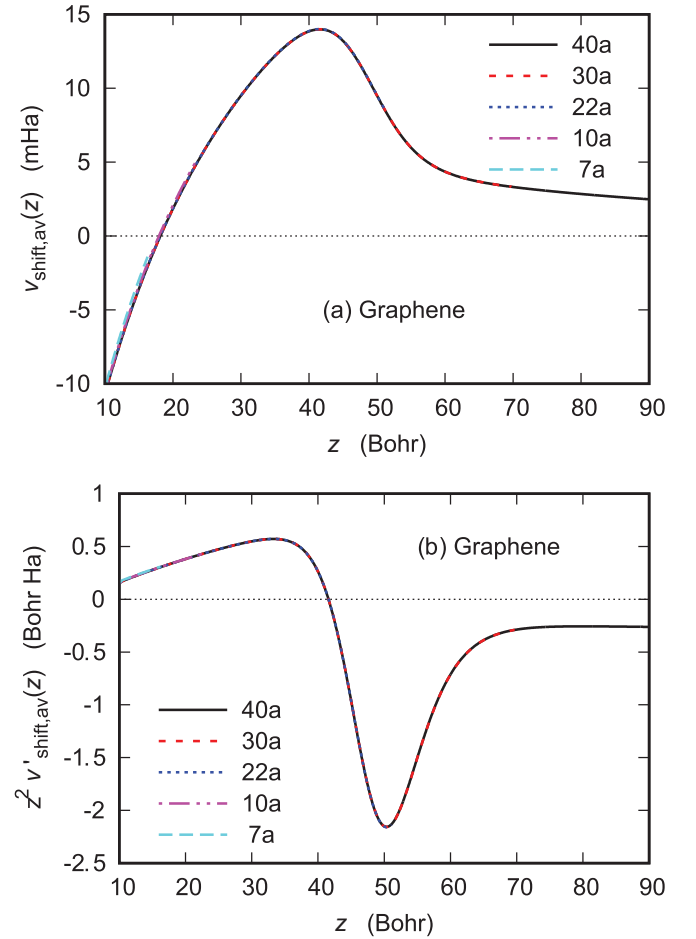
FIG. 14. Convergence of (a) x-y-averaged v_{Slater}, Eq. (29), and (b) its first derivative with respect to z with the width of vacuum d. All results have been obtained with the SE scheme. For $z < 5$ Bohr, the potentials of panel (a) can not be distinguished from the result in Fig. 10(a).

FIG. 15. Convergence of (a) x-y-averaged v_{shift}, Eq. (34), and (b) its first derivative with respect to z with the width of vacuum d. All results have been obtained with the 24×24 $\boldsymbol{k}$-point grid and the SE scheme. For $z < 10$ Bohr, both the potentials and their derivatives can not be distinguished from the corresponding results in Fig. 12.

structure in v_{shift}, is obvious. On the other hand, v_x^{KLI} is quite close to $-1/z$ for the largest z values displayed in Fig. 16. This agreement is, however, produced by a fortuitous error cancellation between v_{Slater} and v_{shift}. Due to the supercell geometry v_{Slater} has a vanishing derivative in the middle of the vacuum [compare Fig. 11(b)] and is therefore more attractive than $-1/z$ in this region. At the same time, v_{shift} has a repulsive $1/z$-behavior for large z (compare Fig. 15).

An analogous comparison for a 6-layer Si(111) slab is given in Fig. 17. Again v_{Slater} is very close to $-1/z$ as soon as one is sufficiently far outside the surface (the outermost layer of atoms is located at $z \approx 8.9$ Bohr). The total EXX/KLI potential, however, differs dramatically from $-1/z$ in the complete range displayed. While v_{shift} does not show any peak structure, its depth dominates over that of v_{Slater} for quite large z.

E. Work function, band energies

In view of the early convergence of v_{Slater} and v_{shift} with d it is no surprise that the corresponding Fermi energy is equally invariant (see Fig. 18). ϵ_F directly reflects the error

in the normalization of v_{shift}, resulting from application of (37) to the discrete numerical $\boldsymbol{k}$-point grid (the error amounts to about 0.06 eV in the case of the 8×8 grid). Since the total electrostatic potential has been normalized to zero in the middle of the vacuum in this work, ϵ_F is identical with the work function [61,62]. Figure 18 thus confirms the large EXX/KLI work function for graphene reported in Ref. [12]. In fact, the work function has even been slightly underestimated in Ref. [12], where the normalization of the EXX/KLI potential was based on the assumption that v_{shift} is negligible for $z \gtrsim 8$ Bohr.

Figure 18 also supports the reliability of the vacuum width of $d = 7a$ used in Ref. [12]. Even the Fermi energy emerging from $d = 5a$ differs by no more than 15 meV from the converged result.

The early convergence of ϵ_F is not restricted to graphene. Table I provides analogous data for a 6-layer Si(111) slab. The difference of about 1 mHa between the converged Fermi energy (obtained from a very wide vacuum and a high resolution $\boldsymbol{k}$-point grid) and the ϵ_F from a standard vacuum and coarse $\boldsymbol{k}$-point grid demonstrates that EXX/KLI calculations can be performed in a computationally efficient way in practice.
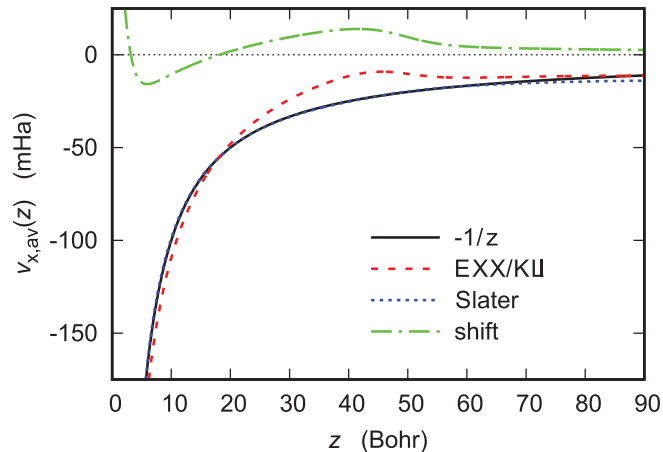
FIG. 16. x-y-averaged v_x^{KLI}, Eq. (28), of graphene in comparison to $-1/z$ (32 × 32 $\boldsymbol{k}$-point grid, CR scheme).

FIG. 18. Fermi energy ϵ_F of graphene: convergence with vacuum width d for different $\boldsymbol{k}$-point grids. Lines are drawn to guide the eye.

While the work function is sensitive to the overall normalization of the potential, many other quantities are not. As an example, Fig. 19 shows the band energies of graphene at the Γ-point as functions of d, normalized to the highest valence band energy. Similar to ϵ_F, the occupied and lowest unoccupied bands are converged already for $d = 5a$. The more delocalized higher states start to become affected as soon as their spatial extension is of the same size as d. Moreover, the transition energies between the bands are completely independent of the $\boldsymbol{k}$-point sampling: already the 8×8 grid gives converged results.

The insensitivity of the band energies to the width of the vacuum is not restricted to the Γ-point, as demonstrated in Fig. 20. The occupied bands obtained with $d = 40a$ are indistinguishable from those resulting from the quite moderate vacuum of $d = 4a$, and even the lowest unoccupied bands are close. Note that the band energies in Fig. 20 are not normalized to each other, but rather represent the data in absolute normalization.

The EXX/KLI Fermi energies obtained with the extension scheme are compared with corresponding LDA and GGA values as well as with experimental work functions in Table II.

In addition to graphene, Si(111) slabs of different thickness are included. Table II first of all demonstrates that plane-wave-based EXX/KLI calculations can be performed for rather thick slabs and reasonably wide vacua, if the extension scheme is combined with moderate cutoff energies. At the same time, the results for the Si(111) slabs are in line with the overestimation of the experimental work function by the EXX/KLI approach observed for graphene. The EXX/KLI work function of 6.53 eV obtained for the 18-layer slab should already be close to the extrapolated value for infinite slab thickness, but is far beyond the experimental work function of the (111) surface of bulk Si. It seems worthwhile to emphasize that this deviation can not be explained by the neglect of relaxation and surface reconstruction in the present work, since both effects reduce the work function of Si(111) by less than 0.3 eV [66].

One can explicitly verify that the depth of the exchange potential inside the slab is responsible for this large work function. The EXX/KLI potential inside graphene is on average about 5.4 eV deeper than its LDA counterpart, as Fig. 21(a)

FIG. 17. x-y-averaged v_x^{KLI}, Eq. (28), of a 6-layer Si(111) slab with $d = 82a/\sqrt{3}$ in comparison to $-1/z$ (32 × 32 $\boldsymbol{k}$-point grid, CI scheme).
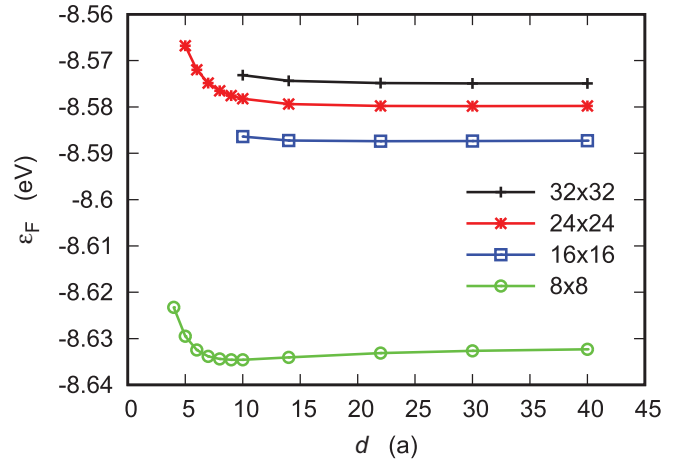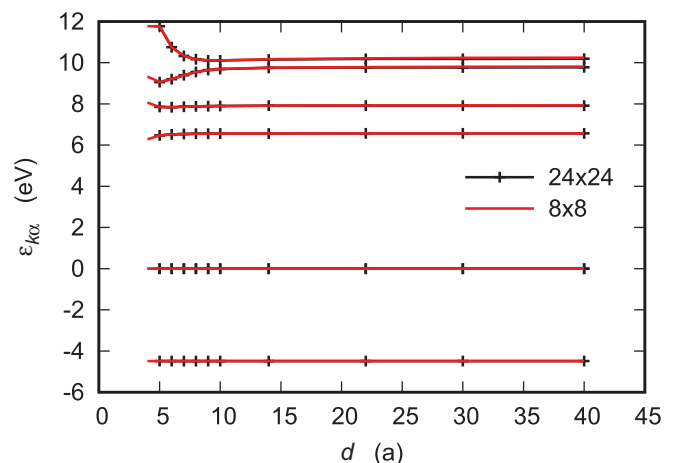

FIG. 19. EXX/KLI band energies $\epsilon_{k\alpha}$ of graphene at Γ-point: convergence with vacuum width d for different $\boldsymbol{k}$-point grids. The eigenvalues are normalized to the highest valence-band energy. Lines are drawn to guide the eye.
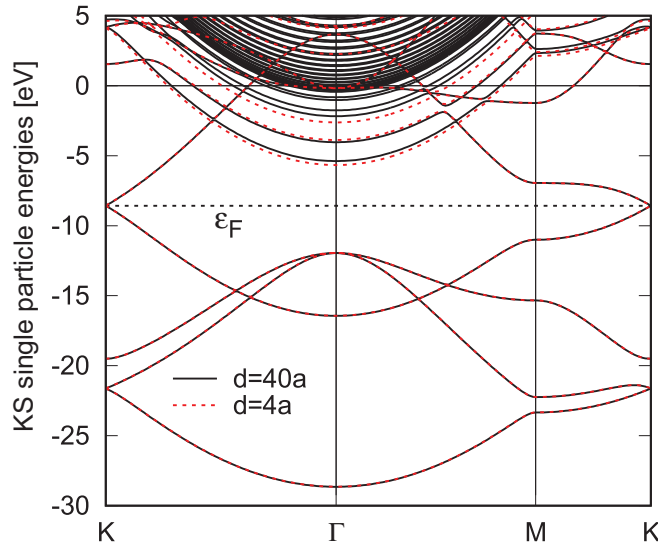
FIG. 20. EXX/KLI band structure of graphene: convergence with vacuum width d.

shows. Similarly, one extracts a difference in well depth of roughly 3 eV for the 6-layer Si(111) slab from Fig. 21(b). Both numbers are in good agreement with the differences between the corresponding work functions in Table II.
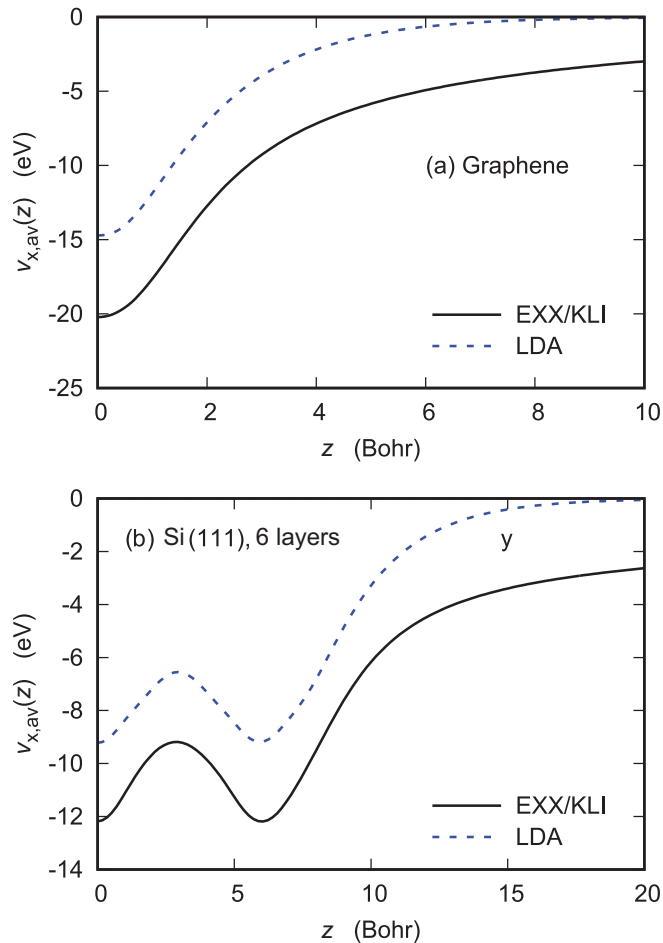

FIG. 21. xy-averaged exchange potential: EXX/KLI result versus LDA (x-only) for (a) graphene and (b) a 6-layer Si(111) slab.

Table II also indicates the role of correlation. In the case of LDA and GGA calculations inclusion of the correlation potential enhances the work function of all slabs considered by more than 1 eV and the same is true if LDA or GGA correlation is added to the EXX/KLI exchange potential (for instance, LDA correlation leads to an increase of 1.38 eV in the case of graphene). This observation should, however, not be interpreted as a proof that the correlation potential necessarily increases the work function. As Fig. 21 shows, it is primarily the asymptotics of the xc potential, which determines the well depth of the total KS potential. Moreover, there are indications [10] that a more accurate correlation potential such as the orbital-dependent RPA will lead to a $-1/(4z)$ behavior of the complete xc potential in the case of metals. One can not exclude that a reduced well depth and thus a reduced work function is obtained by inclusion of an appropriate correlation potential also for the present, nonmetallic slabs. However, it seems very unlikely that the correlation potential can come up for as much as 4 eV for graphene and 2 eV for Si(111). Consequently, the rather large EXX/KLI work functions point at a deficiency of the KLI approximation in the asymptotic region of nonjellium slabs.

VII. SUMMARY AND CONCLUSIONS

In this work, it has been demonstrated that EXX-PWPP calculations in the KLI approximation can be performed for rather thick slabs and very wide vacua, if a real-space extension of the Bloch states into the vacuum is applied. The extension scheme introduced in Sec. III is robust, i.e., insensitive to the transition point between the raw numerical states and their analytical extension, and efficient, since (i) only few in-plane $\boldsymbol{G}$-vectors need to be included in the extension and (ii) the corresponding amplitudes can be accurately determined already for moderate plane-wave cutoff energies. The matching procedure ensures a high degree of continuity of the states, in particular, if the next-to-leading order contribution to the asymptotic form of the states is properly included in the extension. The resulting 3D periodic states mimic the states of a single slab as much as possible. They deviate from the exact solutions of the supercell problem only in the middle of the vacuum, where the exact states have a vanishing derivative with respect to z (compare Fig. 1 of Ref. [12]).

On this basis it has been verified that the Slater potential obtained by PWPP calculations is close to $-1/z$ in an extended region far outside the slab and far from the middle of the vacuum, as predicted in Ref. [12]. However, the results also reveal that the second component of the EXX/KLI potential, the orbital-shift term, is still sizable in this region. This effect primarily originates from the subtle competition between the states dominating close to the surface and those dominating for $z \to \infty$ in both the numerator and the denominator of the orbital-shift term. This competition can even lead to some structure in the orbital-shift potential far outside the slab. The numerical results also confirm the asymptotic $1/z$ behavior of the orbital-shift potential, predicted in Ref. [56]. The asymptotic behavior of the complete EXX/KLI potential thus deviates from the $-1/z$ decay of the exact EXX potential.

This deviation raises some doubts concerning the well depth of the EXX/KLI potential inside the slab, since the well depth
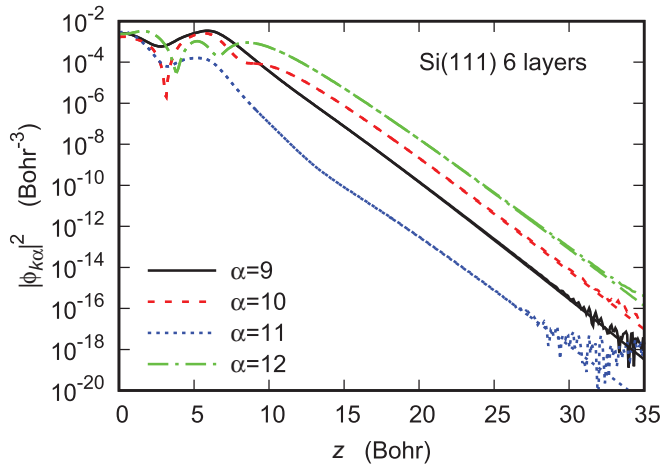
FIG. 22. Densities $|\phi_{k\alpha}(r)|^2$ of valence states of a 6-layer Si(111) slab as functions of z for $x = \frac{9a}{40\sqrt{2}}$ and $y = \frac{\sqrt{6}a}{20}$; $k = \frac{2\pi}{a}(1/\sqrt{32},0)$. Both the original numerical state (23) and its extension by the UI approach are shown ($s = 10^{-8}$ Bohr^{-3}, $d = 12a/\sqrt{3} \approx 70.9$ Bohr, and $E_{\text{cut}} = 320$ Ry).

is intimately linked to the form of the potential for large z. An incorrect well depth would lead to an incorrect work function. If one relies on the identity of the work function with the Fermi energy [61,62], the present EXX/KLI calculations predict a work function for graphene which is 4 eV higher than the experimental value. Similarly, the EXX/KLI Fermi energy of the 18-layer Si(111) slab is 2 eV above the work function of the (111) surface of bulk Si (while an 18-layer slab yields a work function quite close to the bulk value in the case of LDA/GGA calculations).

These results are in obvious contrast to the good agreement of the KLI approximation with the corresponding exact EXX potential in the case of (i) a quasi-two-dimensional electron gas [14] and (ii) EXX-PWPP calculations for graphene with a very moderate vacuum width [12]. The latter comparison, however, did not probe the KLI well depth inside the slab on an absolute scale, since the narrow vacuum did not allow an absolute normalization of the potentials. The agreement of the KLI approximation with the exact EXX potential of nonjellium slabs in an extended region outside the surface remains to be investigated explicitly.

Lacking an implementation of a correlation potential suitable for use with the exact exchange, such as the orbital-dependent RPA [26,29,67–77], the EXX calculations in this work have been performed without any correlation. Clearly, augmentation of the EXX potential by an LDA/GGA correlation potential increases the well depth inside the slab even further and thus enhances the work function. While the same need not be the case for a more suitable correlation potential, it is difficult to conceive that a correlation potential can lower the work function of graphene by as much as 4 eV. The results thus hint at a failure of the KLI approximation.

Nonetheless, the KLI results allow an examination of the convergence of EXX calculations with respect to the width of the vacuum. After all, the KLI exchange potential features a $1/z$ behavior for very large z and seems to be even more attractive than the exact EXX potential in an extended region outside
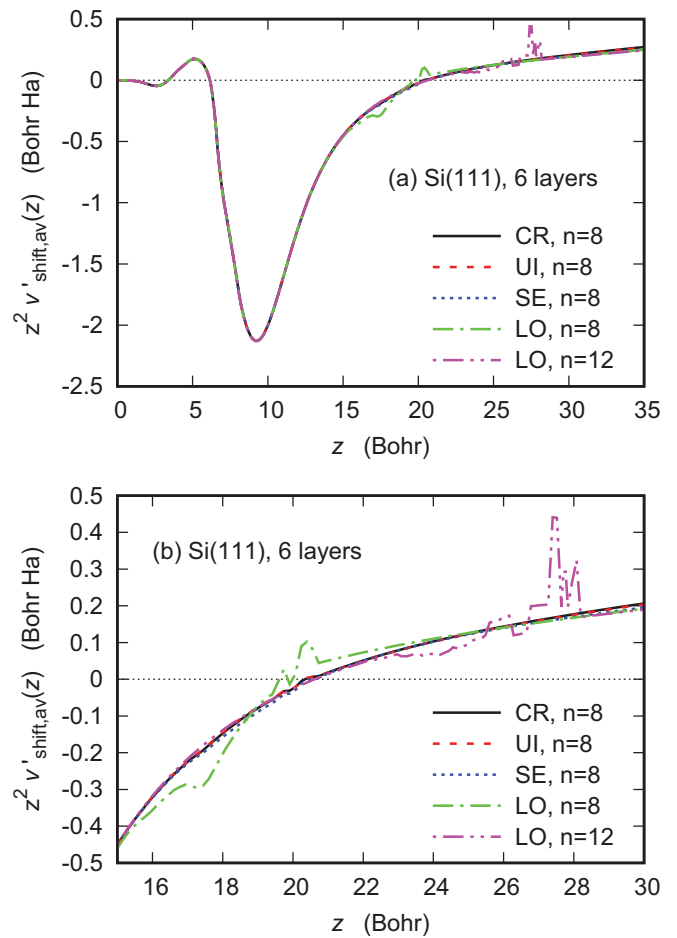

FIG. 23. Derivative of x-y-averaged v_{shift}, Eq. (34), for a 6-layer Si(111) slab with $d = 12a/\sqrt{3}$: comparison of LO, SE, UI, and CR results for $s = 10^{-8}$ Bohr^{-3} ($E_{\text{cut}} = 80$ Ry, 8×8 k-point grid) with LO potential for $s = 10^{-12}$ Bohr^{-3} ($E_{\text{cut}} = 640$ Ry, 8×8 k-point grid). The result of the CI scheme is indistinguishable from the UI data.

the Si(111) surface. The present KLI data demonstrate that the decoupling of neighboring slabs, required for the EXX-PWPP approach to work, sets in for quite moderate separation of the slabs, in spite of the long-range exchange potential. These findings clearly support the applicability of the EXX-PWPP approach to slabs: for moderate width of the vacuum also EXX calculations without the KLI approximation should be feasible, if the extension scheme introduced here is utilized.

ACKNOWLEDGMENTS

APPENDIX: ACCURACY OF EXTENSION SCHEMES FOR SI(111) SLABS

In this Appendix, the information on the extension schemes provided in Secs. VIA–VIC, which focus on graphene, is complemented by corresponding results for Si(111) slabs.
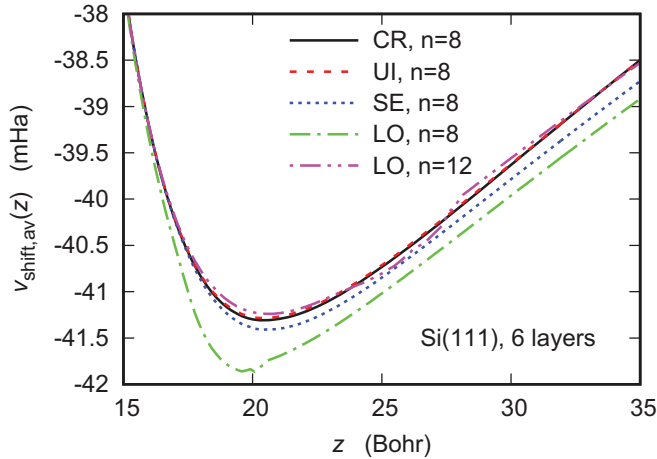
FIG. 24. As Fig. 23 for $v_{\rm shift}$ itself.

1. Extension of Bloch states

Figure 22 demonstrates that the agreement of the extended wave functions with their numerical counterparts is not restricted to graphene (compare Fig. 1).

2. Extension of KLI exchange potential

Figures 23–25 display the orbital-shift potential resulting from the various extensions schemes for a 6-layer Si(111) slab, in analogy to Figs. 6–8. Figure 23 shows the derivative of $v_{\rm shift}$, in particular in the transition region. Two versions of the LO extension are included, differing in their transition thresholds. The potential for $s = 10^{-12}$ Bohr^{-3} serves as rigorous reference result for $z < 22$ Bohr (due to the low s this region is not affected by any manipulation of the states). One can see that the UI and CR extensions (which can not be distinguished on the scale chosen) follow this reference result in and beyond their transition region (which is indicated by the noise in the LO extension with $s = 10^{-8}$ Bohr^{-3}). Even the error in the SE potential is very low. Moreover, in spite of the substantial noise in the LO extension, the LO potential is very close to the more accurate schemes for larger z.

The differences in $\partial_z v_{\rm shift}$ induce a shift in $v_{\rm shift}$ itself, as shown in Fig. 24. Once the transition region is passed,
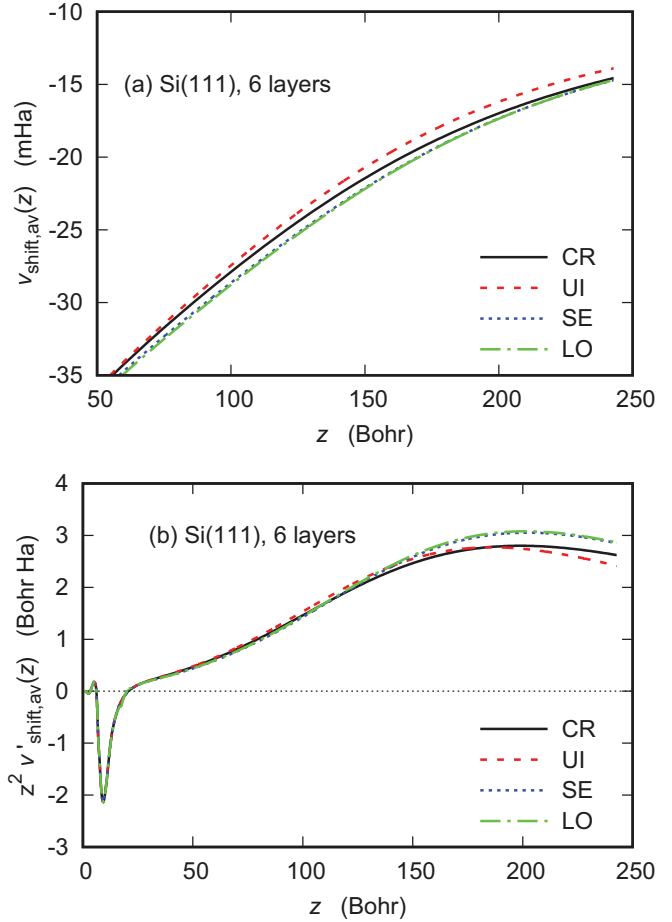

FIG. 25. (a) x-y-averaged $v_{\rm shift}$, Eq. (34), for a 6-layer Si(111) slab with $d = 82a/\sqrt{3}$ and (b) its first derivative: comparison of LO, SE, UI, and CR extensions ($s = 10^{-8}$ Bohr^{-3}, $E_{\rm cut} = 80$ Ry, 8×8 $\boldsymbol{k}$-point grid). The result of the CI scheme is indistinguishable from the UI data.

however, the corresponding potentials resume essentially the same shape: they are just offset by the noise accumulated in the transition region. Figure 24 demonstrates that this offset amounts to no more than 0.5 mHa. The potentials obtained with the various extension schemes remain close to each other even for very large z, as illustrated in Fig. 25.

[1] A. Solomatin and V. Sahni, Ann. Phys. (N.Y.) **259**, 97 (1997).

[2] A. Solomatin and V. Sahni, Phys. Rev. B **56**, 3655 (1997).

[3] Z. Qian and V. Sahni, Phys. Rev. B **66**, 205103 (2002).

[4] Z. Qian and V. Sahni, Int. J. Quantum Chem. **104**, 929 (2005).

[5] Z. Qian, Phys. Rev. B **85**, 115124 (2012).

[6] C. M. Horowitz, C. R. Proetto, and S. Rigamonti, Phys. Rev. Lett. **97**, 026802 (2006).

[7] C. M. Horowitz, C. R. Proetto, and J. M. Pitarke, Phys. Rev. B **78**, 085126 (2008).

[8] C. M. Horowitz, L. A. Constantin, C. R. Proetto, and J. M. Pitarke, Phys. Rev. B **80**, 235101 (2009).

[9] C. M. Horowitz, C. R. Proetto, and J. M. Pitarke, Phys. Rev. B **81**, 121106 (2010).

[10] L. A. Constantin and J. M. Pitarke, Phys. Rev. B **83**, 075116 (2011).

[11] H. Luo, C. M. Horowitz, H.-J. Flad, C. R. Proetto, and W. Hackbusch, Phys. Rev. B **85**, 165133 (2012).

[12] E. Engel, J. Chem. Phys. **140**, 18A505 (2014).

[13] E. Engel, Phys. Rev. B **89**, 245105 (2014).

[14] S. Rigamonti, C. M. Horowitz, and C. R. Proetto, Phys. Rev. B **92**, 235145 (2015).

[15] P. Lazar and M. Otyepka, Phys. Rev. B **91**, 115402 (2015).

[16] L.-H. Ye, Phys. Rev. B **92**, 115132 (2015).

[17] L.-H. Ye, Phys. Rev. B **94**, 035113 (2016).

[18] S. De Waele, K. Lejaeghere, M. Sluydts, and S. Cottenier, Phys. Rev. B **94**, 235418 (2016).

[19] L. A. Constantin, E. Fabiano, J. M. Pitarke, and F. Della Sala, Phys. Rev. B **93**, 115127 (2016).

[20] A. Ruzsinszky, L. A. Constantin, and J. M. Pitarke, Phys. Rev. B **94**, 165155 (2016).

[21] J. D. Talman and W. F. Shadwick, Phys. Rev. A **14**, 36 (1976).

[22] P. Rinke, A. Qteish, J. Neugebauer, C. Freysoldt, and M. Scheffler, New J. Phys. **7**, 126 (2005).

[23] A. Qteish, A. I. Al-Sharif, M. Fuchs, M. Scheffler, S. Boeck, and J. Neugebauer, Comput. Phys. Commun. **169**, 28 (2005).

[24] P. Rinke, M. Scheffler, A. Qteish, M. Winkelnkemper, D. Bimberg, and J. Neugebauer, Appl. Phys. Lett. **89**, 161919 (2006).

[25] S. Sharma, J. K. Dewhurst, and C. Ambrosch-Draxl, Phys. Rev. Lett. **95**, 136402 (2005).

[26] M. Grüning, A. Marini, and A. Rubio, J. Chem. Phys. **124**, 154108 (2006).

[27] P. Carrier, S. Rohra, and A. Görling, Phys. Rev. B **75**, 205126 (2007).

[28] J. Spencer and A. Alavi, Phys. Rev. B **77**, 193110 (2008).

[29] J. Harl and G. Kresse, Phys. Rev. B **77**, 045136 (2008).

[30] J. Harl and G. Kresse, Phys. Rev. Lett. **103**, 056401 (2009).

[31] E. Engel and R. N. Schmid, Phys. Rev. Lett. **103**, 036404 (2009).

[32] X. Wu, A. Selloni, and R. Car, Phys. Rev. B **79**, 085102 (2009).

[33] E. Engel, Phys. Rev. B **80**, 161205(R) (2009).

[34] J. Harl, L. Schimka, and G. Kresse, Phys. Rev. B **81**, 115126 (2010).

[35] M. Greiner, P. Carrier, and A. Görling, Phys. Rev. B **81**, 155119 (2010).

[36] E. J. Bylaska, K. Tsemekhman, S. B. Baden, J. H. Weare, and H. Jonsson, J. Comput. Chem. **32**, 54 (2011).

[37] M. Betzinger, C. Friedrich, S. Blügel, and A. Görling, Phys. Rev. B **83**, 045105 (2011).

[38] T. W. Hollins, S. J. Clark, K. Refson, and N. I. Gidopoulos, Phys. Rev. B **85**, 235126 (2012).

[39] M. Betzinger, C. Friedrich, A. Görling, and S. Blügel, Phys. Rev. B **85**, 245124 (2012).

[40] M. Betzinger, C. Friedrich, and S. Blügel, Phys. Rev. B **88**, 075130 (2013).

[41] H. Schulz and A. Görling, in *Frontiers and Challenges in Warm Dense Matter*, edited by F. Graziani, M. P. Desjarlais, R. Redmer, and S. B. Trickey, Lecture Notes in Computational Science and Engineering (Springer, Berlin, 2014), Vol. 96, p. 87.

[42] J. Klimes and G. Kresse, J. Chem. Phys. **140**, 054516 (2014).

[43] T. Fukazawa and H. Akai, J. Phys.: Condens. Matter **27**, 115502 (2015).

[44] F. Tran, P. Blaha, M. Betzinger, and S. Blügel, Phys. Rev. B **94**, 165149 (2016).

[45] W. Zhu, L. Zhang, and S. B. Trickey, J. Chem. Phys. **145**, 224106 (2016).

[46] M. C. Payne, M. P. Teter, D. C. Allan, T. A. Arias, and J. D. Joannopoulos, Rev. Mod. Phys. **64**, 1045 (1992).

[47] J. R. Chelikowsky, M. Schlüter, S. G. Louie, and M. L. Cohen, Solid State Commun. **17**, 1103 (1975).

[48] J. B. Krieger, Y. Li, and G. J. Iafrate, Phys. Lett. A **146**, 256 (1990).

[49] D. M. Bylander and L. Kleinman, Phys. Rev. Lett. **74**, 3660 (1995).

[50] D. M. Bylander and L. Kleinman, Phys. Rev. B **52**, 14566 (1995).

[51] A. Görling, Phys. Rev. B **53**, 7024 (1996).

[52] M. Städele, J. A. Majewski, P. Vogl, and A. Görling, Phys. Rev. Lett. **79**, 2089 (1997).

[53] E. Engel (unpublished).

[54] P. M. Morse and H. Feshbach, *Methods of Theoretical Physics* (McGraw-Hill, New York, NY, 1953).

[55] See Supplemental Material at http://link.aps.org/supplemental/10.1103/PhysRevB.97.155112 for further details on the iterative solution of Eq. (13).

[56] E. Engel, Phys. Rev. B **97**, 075102 (2018).

[57] H. J. Monkhorst and J. D. Pack, Phys. Rev. B **13**, 5188 (1976).

[58] A. H. MacDonald, Phys. Rev. B **18**, 5897 (1978).

[59] S. Massidda, M. Posternak, and A. Baldereschi, Phys. Rev. B **48**, 5058 (1993).

[60] B. Wenzien, G. Cappellini, and F. Bechstedt, Phys. Rev. B **51**, 14701 (1995).

[61] N. D. Lang and W. Kohn, Phys. Rev. B **3**, 1215 (1971).

[62] F. K. Schulte, J. Phys. C: Solid State Phys. **7**, L370 (1974).

[63] S. H. Vosko, L. Wilk, and M. Nusair, Can. J. Phys. **58**, 1200 (1980).

[64] J. P. Perdew, A. Ruzsinszky, G. I. Csonka, O. A. Vydrov, G. E. Scuseria, L. A. Constantin, X. Zhou, and K. Burke, Phys. Rev. Lett. **100**, 136406 (2008).

[65] C. Oshima and A. Nagashima, J. Phys.: Condens. Matter **9**, 1 (1997).

[66] C. Sgiarovello, N. Binggeli, and A. Baldereschi, Phys. Rev. B **64**, 195305 (2001).

[67] T. Kotani, J. Phys.: Condens. Matter **10**, 9241 (1998).

[68] T. Kotani, J. Phys.: Condens. Matter **12**, 2413 (2000).

[69] F. Furche, Phys. Rev. B **64**, 195120 (2001).

[70] M. Fuchs and X. Gonze, Phys. Rev. B **65**, 235109 (2002).

[71] T. Miyake, F. Aryasetiawan, T. Kotani, M. van Schilfgaarde, M. Usuda, and K. Terakura, Phys. Rev. B **66**, 245103 (2002).

[72] Y. M. Niquet and X. Gonze, Phys. Rev. B **70**, 245115 (2004).

[73] N. E. Dahlen and U. von Barth, J. Chem. Phys. **120**, 6826 (2004).

[74] N. E. Dahlen and U. von Barth, Phys. Rev. B **69**, 195102 (2004).

[75] H. Jiang and E. Engel, J. Chem. Phys. **127**, 184108 (2007).

[76] F. Furche, J. Chem. Phys. **129**, 114105 (2008).

[77] B. G. Janesko, T. M. Henderson, and G. E. Scuseria, J. Chem. Phys. **130**, 081105 (2009).

[78] I. Duchemin and F. Gygi, Comput. Phys. Commun. **181**, 855 (2010).

Correction: Supplemental Material and the corresponding reference and citation have been added.